Self-Tuning Anti-Sway Control For Shipboard Cranes Providing Combined World and Deck-Frame Compensation

Iain A. Martin[a,*], Rishad A. Irani[a]

[a]Multi-Domain Laboratory, Department of Mechanical and Aerospace Engineering, Carleton University, Ottawa, Ontario, K1S 5B6, Canada

ARTICLE INFO

Keywords:
anti-sway control
shipboard crane
knuckle boom crane
self-tuning control
double pendulum
wind disturbances

Abstract

This paper presents a novel self-tuning anti-sway control system for shipboard cranes that provides full, six degree-of-freedom (DOF) motion compensation with respect to both the world (ocean) coordinate frame and the ship deck coordinate frame. The system can either manually or automatically switch between compensation modes during operation, and is capable of providing anti-sway action while tracking a time-varying operator input. Rather than requiring the operator to provide individual joint control, the entire system can track a simple three-axes Cartesian input from the operator, while simultaneously providing full anti-sway compensation in either coordinate frame.

High-fidelity simulation case studies were performed with a nine-DOF shipboard knuckle boom crane, which included double pendulum dynamics between the hook and payload, in the presence of full six-DOF ship motion at sea-state six. The self-tuning anti-sway system showed at least a 92.70% reduction in payload tracking error when the corresponding compensation mode (either deck or world-frame) was activated, a significant reduction in undesired payload motion. Wind disturbances were added to the simulation using the Dryden wind model, where the system showed a maximum decrease in performance of only 0.73%; additional tests were run with self-tuning disabled, which resulted in a decrease in performance of up to 101%, indicating self-tuning is highly effective at minimizing the effect of wind disturbances.

1. Introduction

Shipboard cranes are an important part of many marine operations; however, as the payload is under-actuated, they can are also be extremely hazardous. Ship motion can cause unexpected payload behaviour, which, for an operator standing on the deck, can be difficult to predict or react to. Additionally, high degree-of-freedom (DOF) cranes in use by industry, such as knuckle boom cranes, typically require the operator to control each actuator independently, which can cause further difficulty controlling payload motion in the presence of ship motion. Therefore, this work focuses on the development of an anti-sway control system to limit unexpected payload motion for a 9-DOF shipboard knuckle boom crane, with the intent to simultaneously provide both full motion compensation and intuitive control for the operator.

The study and design of anti-sway control systems for cranes have been of great interest to researchers over the past several decades. Ramli et al. conducted a thorough review of general crane control systems in 2017 [20], where over seventeen different types of crane controllers were discussed. The control strategies used by researchers have varied from the industry-standard proportional-integeral-derivative (PID) controllers to more advanced nonlinear sliding-mode controllers, fuzzy logic controllers and neural networks. Conclusions made by Ramli et al. were that the majority of existing research has focused on gantry and overhead cranes with limited work on tower or rotary cranes, and that the consideration of the hook and payload as a double-pendulum system has received little consideration.

In the past few years, the focus of much shipboard crane research has been on adaptive and robust controllers, often applied to simplified, low-DOF systems. Considering a planar offshore container crane, Ismail et al. [5] in 2015 developed a robust sliding mode controller designed to handle uncertain disturbances such as wind gusts. A 3-DOF offshore container crane was considered by Ngo et al. [16, 15], who developed a fuzzy-tuned sliding mode controller to provide anti-sway control. Qian and Fang [17, 18] also considered the planar offshore boom crane and developed a nonlinear learning controller. Qian [19] later considered the 3-DOF container crane and developed an adaptive learning controller for anti-sway control. In 2017, Kim and Park [6] designed a linear controller for a linearized 5-DOF container

*Corresponding author
IainMartin@cmail.carleton.ca (I.A. Martin); Rishad.Irani@carleton.ca (R.A. Irani)
ORCID(s): 0000-0001-6961-5861 (I.A. Martin); 0000-0003-2854-001X (R.A. Irani)

crane. In 2018, Sun et al. [21] considered a planar boom crane and developed an energy-based nonlinear controller, while Lu et al. [9] developed a nonlinear controller for the 3-DOF boom crane. Once again considering a simplified model of a knuckle boom crane, both Wang et al. [27] and Tysse and Egeland [24] developed anti-sway control systems, where the simplified model only considered the mass and inertia of the crane base, boom, jib and payload, and none of the other crane components.

In 2019, Sun et al. [22] considered the three-DOF container crane and implemented a controller that used a observer to obtain velocity feedback. Also in 2019, Sun et al. [23] included double-pendulum dynamics in a control system for the planar container crane. Kim and Hong [7] considered a 4-DOF offshore container crane and developed an adaptive sliding mode controller. Again considering the planar offshore boom crane, Yang et al. [28] developed a neural-network based adaptive controller and Lu et al. [8] applied nonlinear coordination control. Tysse and Egeland [25] developed an anti-sway controller for a knuckle boom crane using a Lyapunov-based pendulum damping and nonlinear MPC control system. The anti-sway control system developed by Tysse and Egeland did not consider the dynamics of the crane itself, only the interaction between the crane tip and the payload. In 2020, Guo and Chen [4] considered a two-DOF planar shipboard gantry crane and developed a fault-tolerant fuzzy robust controller.

For a more thorough review of shipboard crane anti-sway systems, the reader is referred to the review published by Cao and Li in 2020 [1]. Cao and Li found that the majority of existing work focuses on two or three-DOF dynamic models for planar, 2D cases, and that consideration of high-DOF cranes is lacking in the current literature. Additional conclusions by Cao and Li are that few researchers consider time-varying payload trajectories or the double pendulum effects of a separate hook and payload. Since Cao and Li's review, in 2021 Wang et al. [26] considered a 3D shipboard boom crane and showed the effectiveness of a mechanical damping device to reduce payload sway. Zanjani and Mobayen [29] considered a 3-DOF offshore gantry crane, and provided anti-sway control with a global sliding mode controller. Martin and Irani [11] considered a shipboard 5-DOF gantry and 6-DOF knuckle boom crane, developing a sliding mode controller and anti-sway trajectory modification system that provided anti-sway control in the deck coordinate frame tracking real-time, time-varying trajectories. Martin and Irani extended their control system to include a 7-DOF knuckle boom crane in [10].

In addition to the limitations identified by Cao and Li, few researchers consider the impact of an operator-in-the-loop with the anti-sway control system; as up to 70% of marine accidents can be attributed to human error [3] and the operator will provide real-time input to the system, it is important to design an anti-sway control system that not only provides effective sway reduction, but also provides intuitive control for the operator. Therefore, the intention of the current work is to approach the anti-sway control problem from a different angle than typically seen in literature, with a focus on operator interaction and full motion compensation for a high-DOF, high-fidelity system, rather than the more standard non-linear control approach for simplified systems. The current work is therefore unique from the literature as it, building upon the work presented in [10], contributes a novel anti-sway control system that:

- Can provide both full 6-DOF deck-frame and ocean-frame motion compensation, switching smoothly between each autonomously or at the will of the operator; to the author's knowledge, it is the first such anti-sway control system to be presented in the literature;
- Is capable of operating with real-time input from an operator mapped to an intuitive three-axes Cartesean control scheme, while can also be tasked to follow an time-varying, autonomous, pre-defined trajectory;
- Enhances the self-tuning system used in [10] to account for wind disturbances;
- Is applied to a 9-DOF shipboard knuckle boom crane, which includes double-pendulum dynamics between the hook and payload.

As the system developed in this work is designed from the ground-up for real-time control and operator interaction of a high-DOF marine crane with both deck and ocean-frame anti-sway compensation, to the author's knowledge no suitable comparison exists in the literature for a comparative study. Instead, a comparative study will be performed demonstrating the utility of the self-tuning in the anti-sway system in the presence of wind disturbances and a variable payload mass. Additionally, due to the complexity of developing a suitable, laboratory-scale 6-DOF motion platform and 9-DOF knuckle boom crane, this work presents case studies performed purely in a high-fidelity simulation, and hardware testing is left for future work. A thorough human factors study of the anti-sway system is also left for future work.

Section 2 provides an overview of the 9-DOF knuckle boom crane, and Section 3 outlines the operation of the anti-sway control system. Section 4 provides the simulation case studies, and Section 5 presents the conclusions.

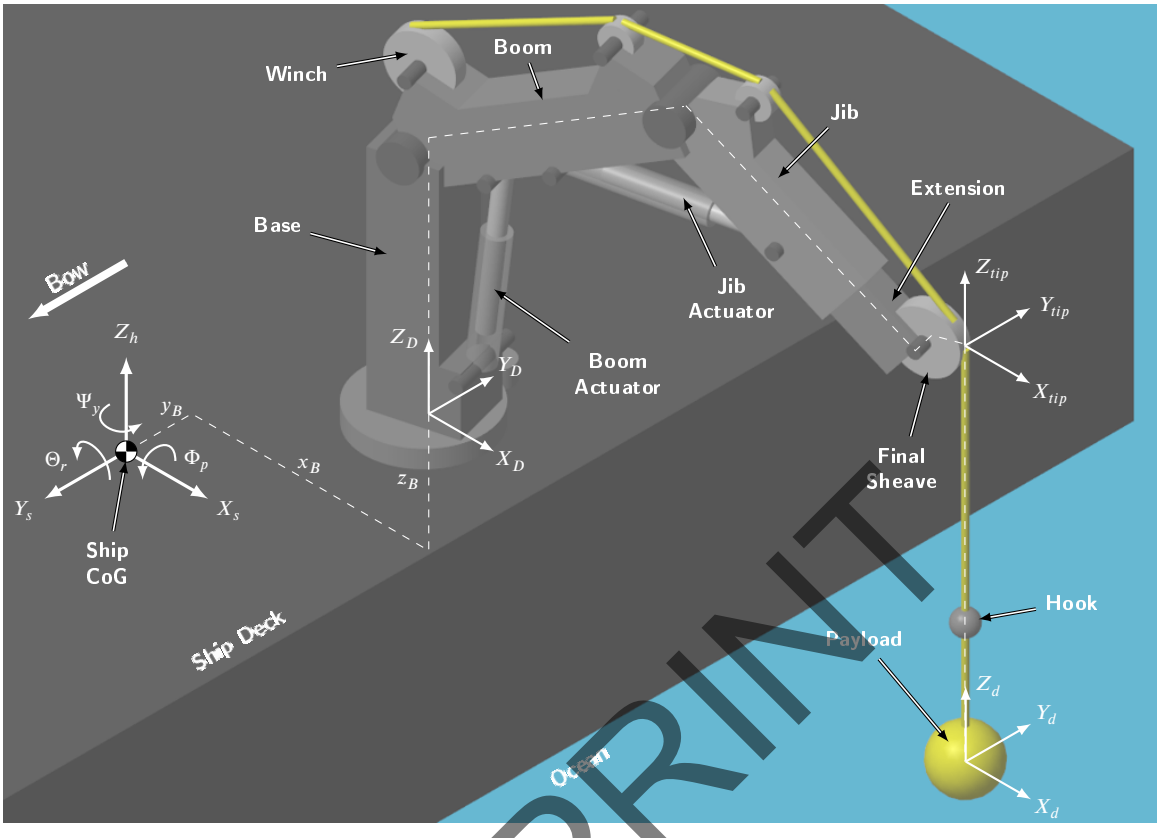

Figure 1: A 3D schematic of the knuckle boom crane showing the major coordinate frames and crane components.

2. 9-DOF Knuckle Boom Crane

The crane used in this work to demonstrate the anti-sway system is a 9-DOF knuckle boom crane, chosen for its relative complexity compared to other types of marine cranes; however, the system is generalized and can be applied to any type of marine crane, such as gantry and boom cranes.

Figure 1 shows a simple 3D schematic of the knuckle boom crane aboard a ship. At the ship's center of gravity (CoG), an IMU measures the surge Y_s, sway X_s and heave Z_h of the ship, along with the roll angle Θ_r, pitch angle Φ_p and yaw angle Ψ_y. Note that the resulting CoG coordinate system is left-handed, as is common in marine applications.

The base of the crane rotates about a deck-fixed coordinate frame XYZ_D, located at a position vector $\mathbf{x}_B = \begin{bmatrix} x_B & y_B & z_B \end{bmatrix}^T$ relative to the ship's CoG. Note that, to comply with standard dynamics and robotics conventions, XYZ_D is a right-handed coordinate system, with Y_D in the opposite direction relative to Y_s. The crane tip is defined as the fall point of the cable from the final sheave, at which point the coordinate system XYZ_{tip} is assigned, where the orientation of XYZ_{tip} is aligned with XYZ_D. The desired position of the payload in the deck coordinate frame, specified by the operator, is given by XYZ_d.

Figure 2 shows the nine degrees of freedom of the crane. The base of the crane rotates relative to the deck coordinate frame XYZ_D by an angle θ_0 about the Z_D axis. The displacements d_1, d_2 and d_3 correspond to the boom actuator, jib actuator and extension, respectively, and l_8 is the cable length between the crane tip and hook. Together, the five degrees of freedom $\mathbf{q} = \begin{bmatrix} \theta_0 & d_1 & d_2 & d_3 & l_8 \end{bmatrix}^T$ are all the actuated degrees of freedom of the crane. The sway angles of the cable from the final sheave to the hook are modelled as a universal joint, with θ_6 and θ_7 representing perpendicular rotation angles. Likewise, the sway angles of the cable between the hook and payload are modelled with another universal joint, where θ_9 and θ_{10} are perpendicular rotation angles. All of the sway angles are unactuated. As a universal joint is attached to both the final sheave and the hook, the cable behaves as a double pendulum.

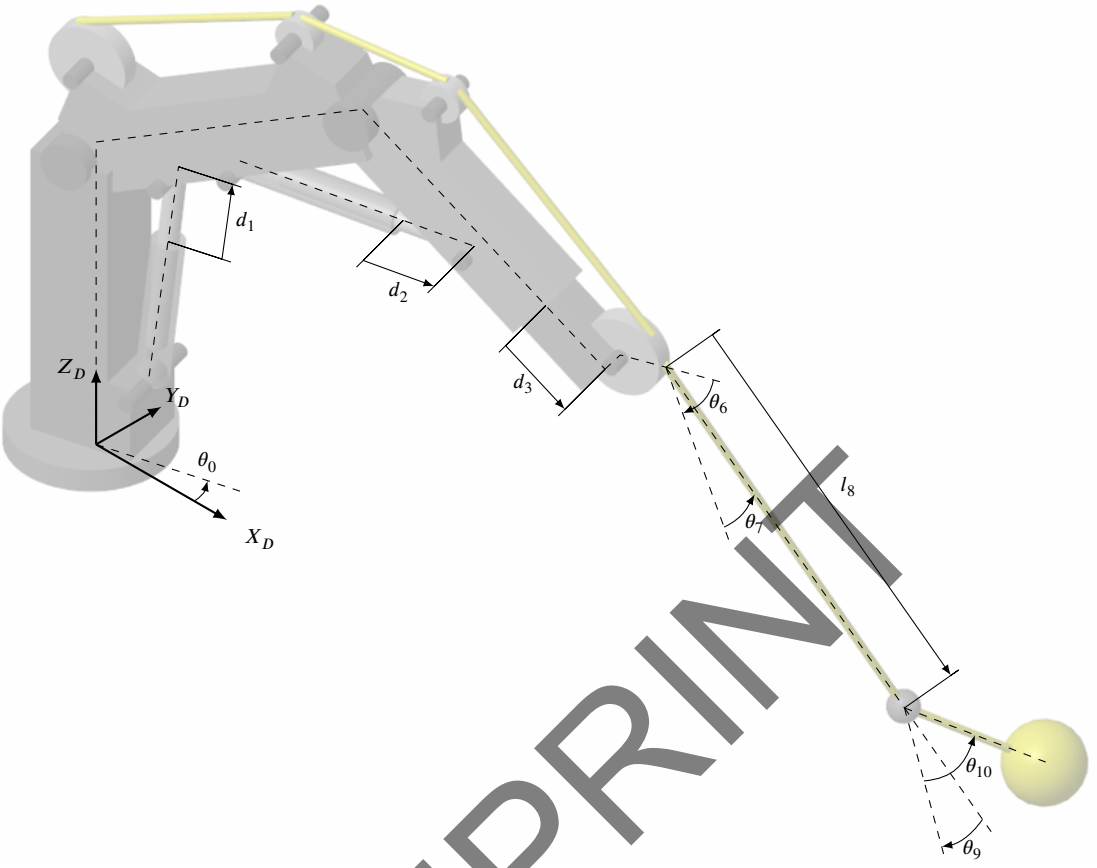

Figure 2: The nine degrees of freedom of the knuckle boom crane. As there are two universal joints on the cable, corresponding to angles $\theta_{6/7}$ and $\theta_{9/10}$, the cable behaves as a double pendulum.

Additional detail on the knuckle boom crane geometry can be found in Appendix A. The forward kinematics used to describe XYZ_{tip} as a function of the crane actuators is provided in Appendix B. Note that to generalize the anti-sway control system to any type of marine crane, one has to define the location of the crane tip XYZ_{tip}, and ensure it is fully actuated.

3. Anti-Sway Control System

Figure 3 shows the high-level structure of the anti-sway control system. The input to the system is a Cartesian 3-vector $\dot{\mathbf{x}}_d = \begin{bmatrix} \dot{x}_d & \dot{y}_d & \dot{z}_d \end{bmatrix}^T$, representing the rate of change of the desired payload position. By using a rate, the input is time-varying and can be provided by an operator using joysticks, or can be chosen to autonomously provide a pre-defined path; it is desired to limit the input to only three axes to provide intuitive control for the operator, such that the payload position can be fully defined using the fewest number of inputs. If the operator attempted to control the system with independent actuator (joint) control, the 9-DOF knuckle boom crane would require five inputs.

The input $\dot{\mathbf{x}}_d$ is integrated by the trajectory integrator to produce the desired payload trajectory $\mathbf{x}_d = \begin{bmatrix} x_d & y_d & z_d \end{bmatrix}^T$. The trajectory integrator uses the tracking error $||x_e||$ from the first optimizer pass to limit the trajectory growth if being driven out of the crane's range of motion. More detail on the trajectory integrator is provided in Appendix C. Once integrated, abrupt changes in joystick position can be smoothed using an optional digital filter.

The smoothed desired trajectory $\mathbf{x}_{ds}$ is then passed to the actuator optimizer for a first optimizer pass. During this pass, the optimizer attempts to find actuator extensions to track $\mathbf{x}_{ds}$ within the set actuator limits $\mathbf{q}_{max/min,1}$. The resulting tracking error $||x_e||$ is passed back to the trajectory integrator. More detail on the actuator optimizer is provided in Section 3.1.

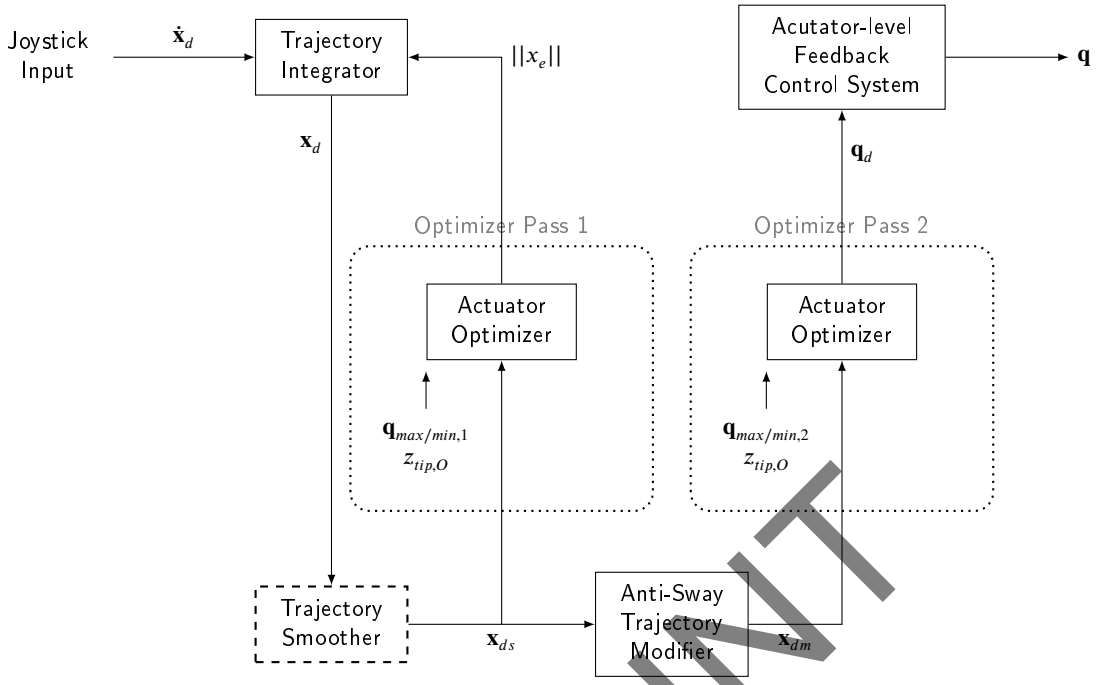

Figure 3: The high-level structure of the anti-sway control system. The trajectory smoother is an optional digital filter.

The smoothed desired trajectory $\mathbf{x}_{ds}$ is also passed to the anti-sway trajectory modifier, which shapes the trajectory to provide anti-sway action. More detail on the anti-sway trajectory modifier is provided in Section 3.2. The modified desired trajectory $\mathbf{x}_{dm}$ is then sent to the actuator optimzier for a second pass to determine appropriate actuator extensions within the actuator limits $\mathbf{q}_{max/min,2}$. The desired actuator setpoints $\mathbf{q}_d$ produced by the optimizer are then used by the actuator-level feedback control system of the crane to produce the actual crane states $\mathbf{q}$.

The system uses two optimizer passes to prevent the crane being driven out of range by the additional motion from the anti-sway trajectory modifier. While the second optimizer pass uses the actual, true actuator limits as $\mathbf{q}_{max/min,2}$, the limits $\mathbf{q}_{max/min,1}$ can be set to be less than the true limits. Therefore, if the trajectory provided by the operator reaches the limits $\mathbf{q}_{max/min,1}$, the trajectory integrator can stop further growth of the trajectory, while allowing the crane to continue providing anti-sway compensation, as the crane has not actually reached its true limits $\mathbf{q}_{max/min,2}$.

3.1. Actuator Optimizer

Figure 4 shows the actuator optimizer, which finds actuator setpoints $\mathbf{q}_d$ to track a desired payload position $\mathbf{x}_d$. If the initial condition of the trajectory integrator was not set to the initial $\mathbf{x}_{initial}$ position of the crane, the initial position can be obtained using the initial actuator extensions $\mathbf{q}_{initial}$ and the forward kinematics of the crane, provided in Appendix D. Adding the initial position to the desired trajectory provides the desired trajectory in the deck frame $\mathbf{x}_{d,deck}$, which is then run through the optimizer subsystem to produced optimized actuator setpoints $\mathbf{q}_{opt}$. To ensure the system can perform fast enough in real-time, the optimizer is run up to a maximum number of iterations n_i. The actuator setpoints are then limited by a saturation function to be in the set range $\mathbf{q}_{max/min}$. The resulting setpoints $\mathbf{q}_d$ are then passed through the forward kinematics to obtain the achieved Cartesian position $\mathbf{x}_{achieved}$, from which the tracking error $\mathbf{x}_e$ is calculated. In this work the system is run at 100 Hz, resulting in a relatively small change in desired payload position between timesteps, for which a value of $n_i = 5$ was found to be suitable.

The actuator optimizer requires a trajectory $\mathbf{x}_{d,tip}$ for the fully actuated crane tip. The mapping of x_d and y_d to the crane tip will be corrected in the anti-sway trajectory modifier, and so at the optimizer stage, $x_{d,tip} = x_d$ and $y_{d,tip} = y_d$. However, z_d, the operator's desired vertical motion for the payload, must be split into two components: the desired tip vertical motion $z_{d,tip}$, and the winch cable length setpoint $l_{8,d}$. Thus, an algorithm mapping $z_{d,tip}$ and $l_{8,d}$ to z_d must be developed.

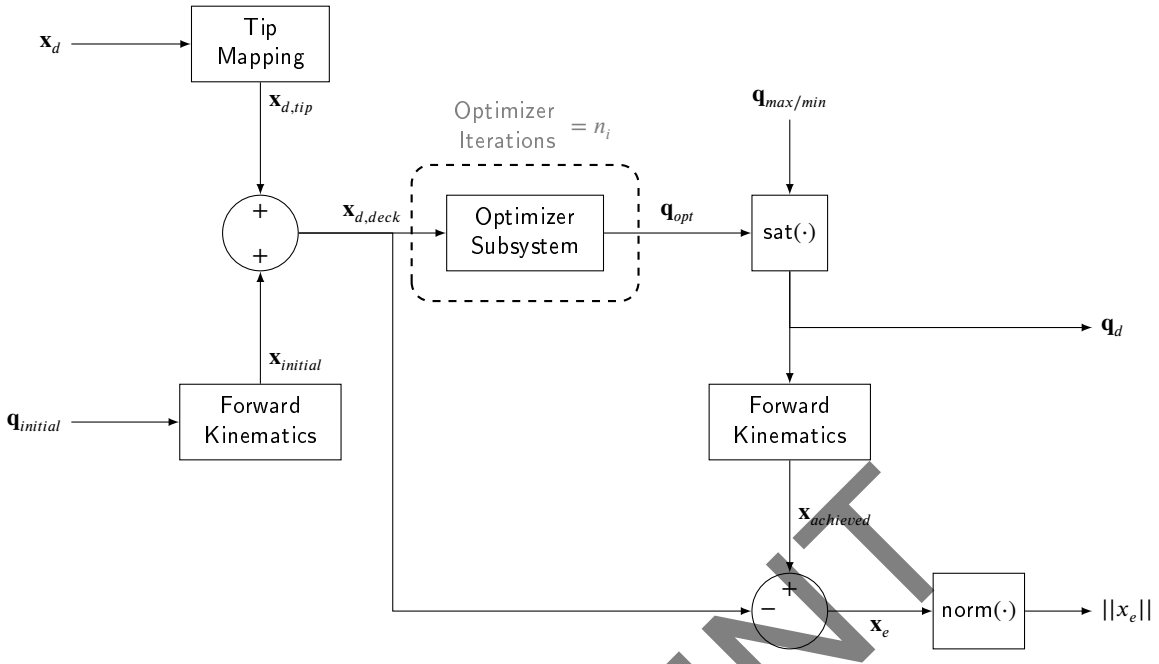

Figure 4: Actuator optimizer system

3.1.1. Tip Mapping

The proposed system distributes the operator's desired vertical motion z_d between the tip $z_{d,tip}$ and cable $l_{8,d}$ based on the boom actuator setpoint and cable length setpoint; as the boom actuator moves towards its endstops, the system will more favour the cable. However, if the cable length decreases such that the hook approaches the sheave, the system will more favour the tip. At the current timestep i, $z_{d,tip}$ and $l_{8,d}$ are

$$z_{d,tip} = \begin{cases} z_{tip,O} & \text{if } ||z_{tip,O}|| > 0 \\ \frac{\dot{z}_d \Delta t}{z_R + 1} & \text{otherwise} \end{cases} \tag{1}$$

$$l_{8,d} = \begin{cases} z_{tip,O} - \dot{z}_d \Delta t & \text{if } ||z_{tip,O}|| > 0 \\ \frac{-\dot{z}_d \Delta t}{z_R + 1} z_R & \text{otherwise} \end{cases} \tag{2}$$

where $z_{tip,O}$ is the vertical tip override, provided by the operator, $\Delta t = \frac{1}{f}$ where f is the operating frequency, and z_R is the cable-tip ratio, given by

$$z_R = z_{R,n} + \frac{z_{R,1} + d_{1,c}}{z_{R,2}} \tag{3}$$

where $z_{R,n}$ is the nominal cable-tip ratio and $d_{1,c}$, the center of the boom actuator's stroke, is $d_{1,c} = 0.5 d_{1,s}$, where $d_{1,s}$ is the stroke of the boom actuator, and

$$z_{R,1} = \begin{cases} \left|\left| \frac{1}{k_1 \ln ||d_{1,d} - d_{1,c}||_{(i-1)}} \right|\right| & \text{if } ||d_{1,d} - d_{1,c}||_{(i-1)} > ||d_{1,d} - d_{1,c}||_{(i-2)} \\ 0 & \text{otherwise} \end{cases} \tag{4}$$

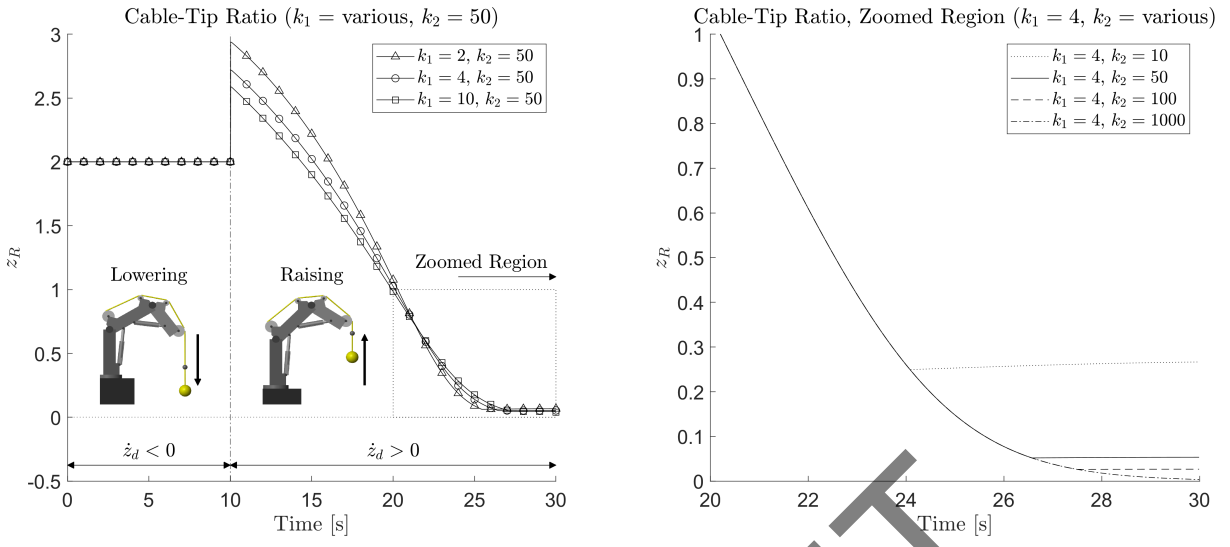

Figure 5: The cable-tip ratio z_R for a range of shaping constants k_1 and k_2. The left-hand figure shows the response of the cable-tip ratio for a variable k_1, with $k_2 = 50$. The right-hand figure shows the response of the cable-tip ratio for a variable k_2, with $k_1 = 4$. Note that the right-hand figure shows a zoomed region of the left-hand figure, as k_2 simply acts to limit the cable-tip ratio.

$$z_{R,2} = \begin{cases} k_2 & \text{if } \left[l_{8,d}\right]_{(i-1)} > l_{8,min} \\ l_{8,min} & \text{if } \left[l_{8,d}\right]_{(i-1)} < l_{8,min} \text{ and } \left[l_{8,d}\right]_{(i-1)} > \left[l_{8,d}\right]_{(i-2)} \\ \dfrac{1}{\ln\left(\left[l_{8,d}\right]_{(i-1)}\right)} & \text{otherwise} \end{cases} \tag{5}$$

where $d_{1,d}$ is the boom actuator setpoint, $l_{8,d}$ is the cable length setpoint, and $l_{8,min}$ is the minimum length of cable below the sheave before the system begins to favour tip motion over cable motion, in this work set to $l_{8,min} = 1$ m.

The constants k_1 and k_2 shape the evolution of the cable-tip ratio z_R during operation; as an example, Figure 5 shows the evolution of z_R for different values of k_1 and k_2 during a simple test, where the desired vertical position z_d of the payload is first lowered for 10 seconds, then raised for 20 seconds. The boom actuator has a stroke of 2 metres, the initial boom actuator extension and cable length are 1.25 metres and 1.5 metres, and the nominal tip ratio is set to $z_{R,n} = 2$. Initially, with the payload being lowered, the boom actuator is moving away from its endstop and towards the center of its stroke, while the cable is also moving away from the sheave; therefore, the cable-tip ratio remains at the nominal value of 2. However, when the payload is raised, the boom actuator is moving away from the center and towards its endstop, and the cable is retracting towards the sheave; therefore, the cable-tip ratio dynamically adjusts. As the cable length is reduced and the hook approaches the sheave, the system reduces the cable-tip ratio, and begins to more-heavily favour motion of the tip. The constant k_1 affects the "slope" of the response of z_R, where a larger value of k_1 results in a more gradual change in z_R. Observing the right-hand side of Figure 5, the value of k_2 acts as limit on the cable-tip ratio, with a higher value of k_2 allowing z_R to more closely approach zero. With the tip mapping defined and the forward kinematics known (see Appendix B), the operation of the optimizer subsystem shown in Figure 4 will be discussed.

3.1.2. Optimizer Subsystem

Figure 6 shows the optimizer subsystem, contained in the overall actuator optimizer shown in Figure 4. The knuckle boom crane used in this study is over-actuated, with four actuators driving the Cartesian position of the crane tip. Therefore, it uses two optimization functions; one keeping the extension actuator fixed, and allowing the jib actuator to move (the *Jib* function), while the other holds the jib actuator fixed and allows the extension to move (the *Extension*

function). Both functions have the same structure:

$$\mathbf{q}_{i+1} = \mathbf{q}_i + \left[\nabla_{Jib}\right]^{-1}\mathbf{f}, \tag{6}$$

$$\mathbf{q}_{i+1} = \mathbf{q}_i + \left[\nabla_{Extension}\right]^{-1}\mathbf{f}, \tag{7}$$

where

$$\mathbf{f} = \begin{Bmatrix} f_1 \\ f_2 \\ f_3 \end{Bmatrix} = \begin{Bmatrix} x_{tip} - x_d \\ y_{tip} - y_d \\ z_{tip} - z_d \end{Bmatrix}, \tag{8}$$

$$\nabla_{Jib} = \begin{bmatrix} \frac{\partial f_1}{\partial \theta_0} & \frac{\partial f_1}{\partial d_1} & \frac{\partial f_1}{\partial d_2} \\ \frac{\partial f_2}{\partial \theta_0} & \frac{\partial f_2}{\partial d_1} & \frac{\partial f_2}{\partial d_2} \\ \frac{\partial f_3}{\partial \theta_0} & \frac{\partial f_3}{\partial d_1} & \frac{\partial f_3}{\partial d_2} \end{bmatrix}, \tag{9}$$

$$\nabla_{Extension} = \begin{bmatrix} \frac{\partial f_1}{\partial \theta_0} & \frac{\partial f_1}{\partial d_1} & \frac{\partial f_1}{\partial d_3} \\ \frac{\partial f_2}{\partial \theta_0} & \frac{\partial f_2}{\partial d_1} & \frac{\partial f_2}{\partial d_3} \\ \frac{\partial f_3}{\partial \theta_0} & \frac{\partial f_3}{\partial d_1} & \frac{\partial f_3}{\partial d_3} \end{bmatrix}, \tag{10}$$

where $\mathbf{f}$ is the cost function, and x_{tip}, y_{tip} and z_{tip} are the coordinates of the crane tip in the deck coordinate frame. Expressions for the terms in equations (8)-(10) are provided in Appendix D.

Initially, the crane will always attempt to move the jib actuator first, unless the extension actuator is already active and $d_3 > 0$. The resulting actuator setpoints $\mathbf{q}_{i+1}$ are converted to a Cartesian coordinates $\mathbf{x}_{d,i+1}$ using the forward kinematics, giving an error e between the desired and achieved positions. If the jib actuator was active and the error above a certain threshold ϵ_2, the system will re-try the optimization with the extension active instead. If the extension is active, or the error was below ϵ_2 the error is then compared to another threshold ϵ_3, where $\epsilon_2 > \epsilon_3$. If the error is greater than ϵ_3 and we have not yet reached the maximum number of iterations n_i, we repeat the optimizer to attempt to reduce the error.

With the actuator optimizer complete, the anti-sway trajectory modifier will be developed.

3.2. Anti-Sway Trajectory Modifier

The proposed anti-sway control systems features two modes of operation: deck-frame compensation and world-frame compensation. In deck-frame compensation, the payload is held stationary with respect to the deck of the mothership, allowing an operator to transfer cargo across the deck without unexpected motion. In contrast, world-frame compensation allows the payload to be held stationary with respect to the ocean, which could be used by an operator for off-board operations. Both compensation modes are combined into a single anti-sway trajectory modifier that can switch smoothly between each, either automatically or manually with input from the operator.

3.2.1. Deck-Frame Compensation

The deck-frame compensation system is based on the system developed in [10], adapted for use with the double pendulum 9-DOF knuckle boom crane. The x and y components of the deck-frame compensator x_{DF} and y_{DF} are

$$x_{DF} = (1 + \xi_x)(l_8 + l_{11})\tan\left(\Theta_r\right) + \Upsilon_x, \tag{11}$$

$$y_{DF} = (1 + \xi_y)(l_8 + l_{11})\tan\left(\Phi_p\right) + \Upsilon_y, \tag{12}$$

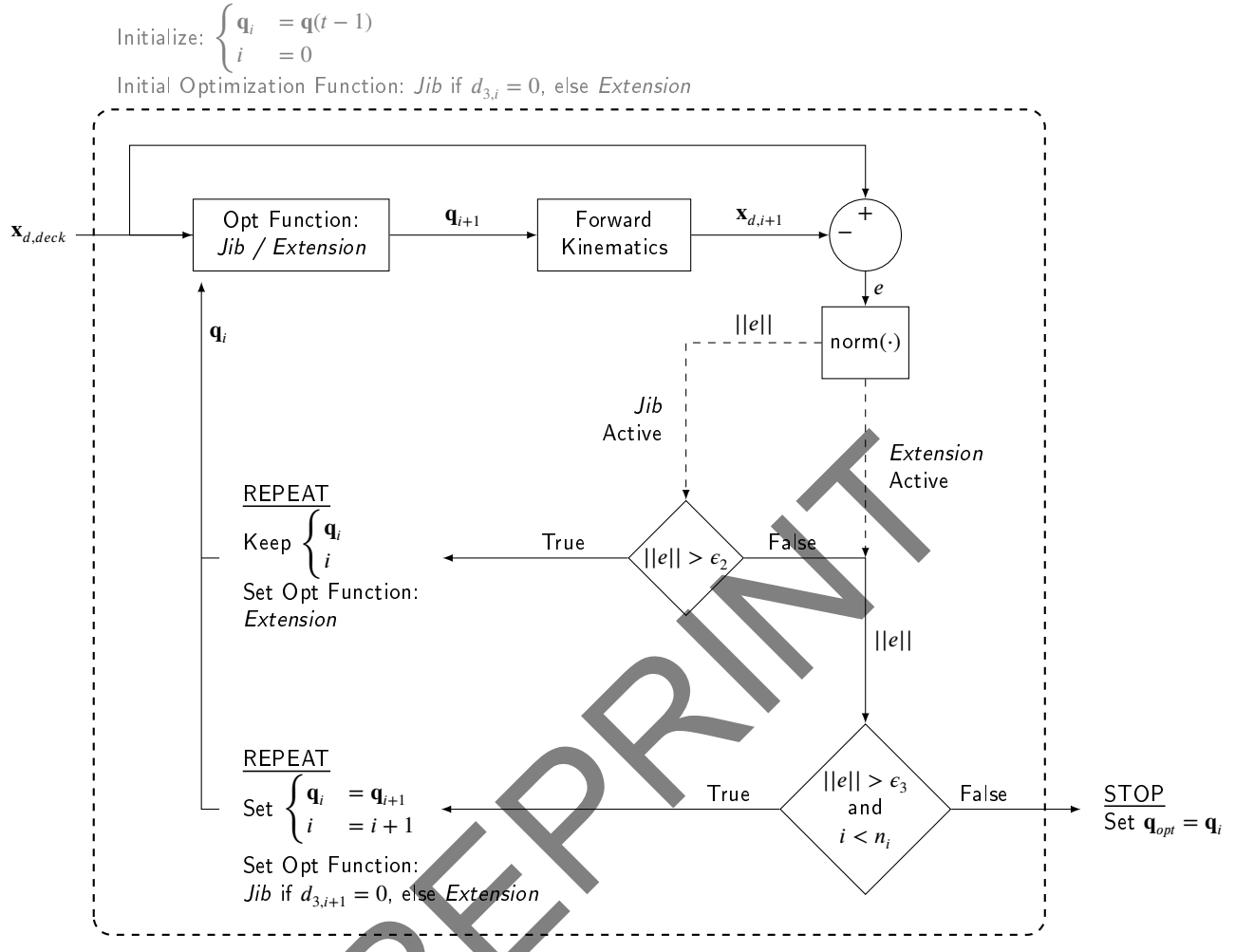

Figure 6: Optimizer subsystem

where ξ_x and ξ_y are dimensionless scaling gains, and Υ_x and Υ_y are offsets. The scaling gains ξ_x and ξ_y are driven by adaption laws,

$$\xi_x = \xi_x' + \begin{cases} -\varrho_x & \text{if } \operatorname{sgn}(e_x) = \operatorname{sgn}(\tan(\Theta_r)) \text{ and } \xi_x > \xi_{x,min} \\ \varrho_x & \text{if } \operatorname{sgn}(e_x) \neq \operatorname{sgn}(\tan(\Theta_r)) \text{ and } \xi_x < \xi_{x,max} \\ 0 & \text{otherwise} \end{cases}, \tag{13}$$

$$\xi_y = \xi_y' + \begin{cases} -\varrho_y & \text{if } \operatorname{sgn}(e_y) = \operatorname{sgn}(\tan(\Phi_p)) \text{ and } \xi_y > \xi_{y,min} \\ \varrho_y & \text{if } \operatorname{sgn}(e_y) \neq \operatorname{sgn}(\tan(\Phi_p)) \text{ and } \xi_y < \xi_{y,max} \\ 0 & \text{otherwise} \end{cases} \tag{14}$$

where $'$ designates the previous timestep, ϱ_x and ϱ_y are the growth rates, e_x and e_y the error between the actual and desired payload position, and $\xi_{x,min}$, $\xi_{x,max}$, $\xi_{y,min}$ and $\xi_{y,max}$ the limits on the scaling gains [10]. The offsets Υ_x and Υ_y have been added in the current work to the deck-frame compensation to aid with disturbance rejection and are driven by adaption laws

$$\Upsilon_x = \Upsilon_x' + \Gamma_x x_e, \tag{15}$$

$$\Upsilon_y = \Upsilon'_y + \Gamma_y y_e, \tag{16}$$

where Γ_x and Γ_y are the growth rates.

As the z component is mapped between $z_{d,tip}$ and $l_{8,d}$ in the actuator optimizer, the z component of the deck-frame compensator is

$$z_{DF} = \frac{1}{\cos(\Theta_r)\cos(\Phi_p)} \tag{17}$$

With the deck-frame compensation functions x_{DF}, y_{DF} and z_{DF} fully defined, the corresponding functions for the world frame x_{WF}, y_{WF} and z_{WF} must be developed.

3.2.2. World-Frame Compensation

To derive the world-frame expressions x_{WF}, y_{WF} and z_{WF}, the transformation matrix ${}^{IMU}T_D$ mapping from the ship's IMU to the deck coordinate frame is first required,

$${}^{IMU}T_D = T_{xyz,IMU} \cdot R_{Yaw} \cdot R_{Pitch} \cdot R_{Roll} \cdot T_{xyz,D} \tag{18}$$

where

$$T_{xyz,IMU} = \begin{bmatrix} 1 & 0 & 0 & X_s \\ 0 & 1 & 0 & -Y_s \\ 0 & 0 & 1 & Z_h \\ 0 & 0 & 0 & 1 \end{bmatrix} \tag{19}$$

$$R_{Yaw} = \begin{bmatrix} \cos(\Psi_y) & -\sin(\Psi_y) & 0 & 0 \\ \sin(\Psi_y) & \cos(\Psi_y) & 0 & 0 \\ 0 & 0 & 1 & 0 \\ 0 & 0 & 0 & 1 \end{bmatrix} \tag{20}$$

$$R_{Pitch} = \begin{bmatrix} 1 & 0 & 0 & 0 \\ 0 & \cos(\Phi_p) & -\sin(\Phi_p) & 0 \\ 0 & \sin(\Phi_p) & \cos(\Phi_p) & 0 \\ 0 & 0 & 0 & 1 \end{bmatrix} \tag{21}$$

$$R_{Roll} = \begin{bmatrix} \cos(-\Theta_r) & 0 & \sin(-\Theta_r) & 0 \\ 0 & 1 & 0 & 0 \\ -\sin(-\Theta_r) & 0 & \cos(-\Theta_r) & 0 \\ 0 & 0 & 0 & 1 \end{bmatrix} \tag{22}$$

$$T_{xyz,D} = \begin{bmatrix} 1 & 0 & 0 & x_B \\ 0 & 1 & 0 & y_B \\ 0 & 0 & 1 & z_B \\ 0 & 0 & 0 & 1 \end{bmatrix} \tag{23}$$

where X_s, Y_s and Z_h are the ship's sway, surge and heave, Ψ_y, Φ_p and Θ_r are the ship's yaw, pitch and roll angles, and x_B, y_B and z_B are the components of the relative position vector between the IMU and the base of the crane. As shown in Figure 1, in the right-handed coordinate system used in this study, the x axis points to port and the y axis points to the stern. Therefore, to correct the left-handed IMU measurements and convert to the right-handed coordinate system, the roll Θ_r and surge Y_s are negated in equations (19) and (22).

As the trajectory modifier operates in the deck-frame, the x and y components of the world-frame compensator x_{WF} and y_{WF} can be obtained by rotating ${}^{IMU}T_D$ into the deck coordinate frame through the reverse rotation sequence,

$$T_{WF,xy} = \left[R_{Roll}\right]^{-1} \cdot \left[R_{Pitch}\right]^{-1} \cdot \left[R_{Yaw}\right]^{-1} \cdot {}^{IMU}T_D, \tag{24}$$

where the first row, fourth column and second row, fourth column entries of matrix $T_{WF,xy}$ will correspond to x_{WF} and y_{WF},

$$\begin{aligned} x_{WF} =& T_{WF,xy}(1,4) \\ =& \left[c(\Psi_y)s(\Phi_p)Y_s + s(\Phi_p)s(\Psi_y)X_s + c(\Phi_p)Z_h\right]s(\Theta_r) \\ &+ \left[c(\Psi_y)X_s - s(\Psi_y)Y_s\right]c(\Theta_r) + x_B, \end{aligned} \tag{25}$$

$$\begin{aligned} y_{WF} =& T_{WF,xy}(2,4) \\ =& -c(\Psi_y)c(\Phi_p)Y_s - s(\Psi_y)c(\Phi_p)X_s + s(\Phi_p)Z_h + y_B, \end{aligned} \tag{26}$$

where $\cos(\cdot)$ and $\sin(\cdot)$ are abbreviated $c(\cdot)$ and $s(\cdot)$, respectively.

For the z component of the world-frame compensator z_{WF}, the vertical motion can be measured at the projected position of the payload in the XY_D plane, as shown in Figure 7, where the projected position in the world frame is defined as

$$T_{Proj,IMU} = {}^{IMU}T_D \begin{bmatrix} 1 & 0 & 0 & x_{tip} - z_{tip}s(\Theta_r) \\ 0 & 1 & 0 & y_{tip} - z_{tip}s(\Phi_p) \\ 0 & 0 & 1 & 0 \\ 0 & 0 & 0 & 1 \end{bmatrix}, \tag{27}$$

where x_{tip}, y_{tip} and z_{tip} are the Cartesian coordinates of the crane tip in the deck coordinate frame, obtained from the forward kinematics in Appendix B. Therefore, the third row, fourth column of matrix $T_{Proj,IMU}$ can be rotated into the deck coordinate frame,

$$T_{Proj,D} = \left[R_{Roll}\right]^{-1} \cdot \left[R_{Pitch}\right]^{-1} \cdot \left[R_{Yaw}\right]^{-1} \cdot \begin{bmatrix} 1 & 0 & 0 & 0 \\ 0 & 1 & 0 & 0 \\ 0 & 0 & 1 & T_{Proj,IMU}(3,4) \\ 0 & 0 & 0 & 1 \end{bmatrix}, \tag{28}$$

giving,

$$\begin{aligned} z_{WF} =& T_{Proj,D}(3,4) \\ =& c(\Theta_r)c(\Phi_p)\Big[c(\Phi_p)^2 z_{tip} + \left[c(\Theta_r)^2 z_{tip} + c(\Theta_r)z_B + (x_B + x_{tip})s(\Theta_r) - z_{tip}\right]c(\Phi_p) \\ &+ (y_B + y_{tip})s(\Phi_p) - z_{tip} + Z_h\Big]. \end{aligned} \tag{29}$$

With the world-frame compensation functions x_{WF}, y_{WF} and z_{WF} fully defined,they will be combined with the corresponding deck-frame functions x_{DF}, y_{DF} and z_{DF}, defined in Section 3.2.1, to develop the full anti-sway system.

3.2.3. Combined Anti-Sway System

Both deck-frame and world-frame compensation can be combined into a single trajectory modifier for the crane tip,

$$x_{dm} = x_d + x_{DF} + S_{WF}(x_{WF,lock} - x_{WF}), \tag{30}$$

$$y_{dm} = y_d + y_{DF} + S_{WF}(y_{WF,lock} - y_{WF}), \tag{31}$$

$$z_{dm} = z_d(z_{DF}) + S_{WF}(z_{WF,lock} - z_{WF}), \tag{32}$$

where x_d, y_d and z_d are the desired payload trajectories (or smoothed desired trajectories x_{ds}, y_{ds} and z_{ds}), and x_{dm}, y_{dm} and z_{dm} are the modified crane tip trajectories, ready to be passed to the actuator optimizer. The elements of the deck-frame compensation x_{DF}, y_{DF} and z_{DF} are given in equations (11), (12) and (17), and the elements of the world-frame compensation x_{WF}, y_{WF} and z_{WF} are given in equations (25), (26) and (29).

Once world-frame compensation is activated, the system "locks" the current world-frame compensation values in $x_{WF,lock}$, $y_{WF,lock}$ and $z_{WF,lock}$. World-frame compensation is applied by adding to the tip trajectory the relative

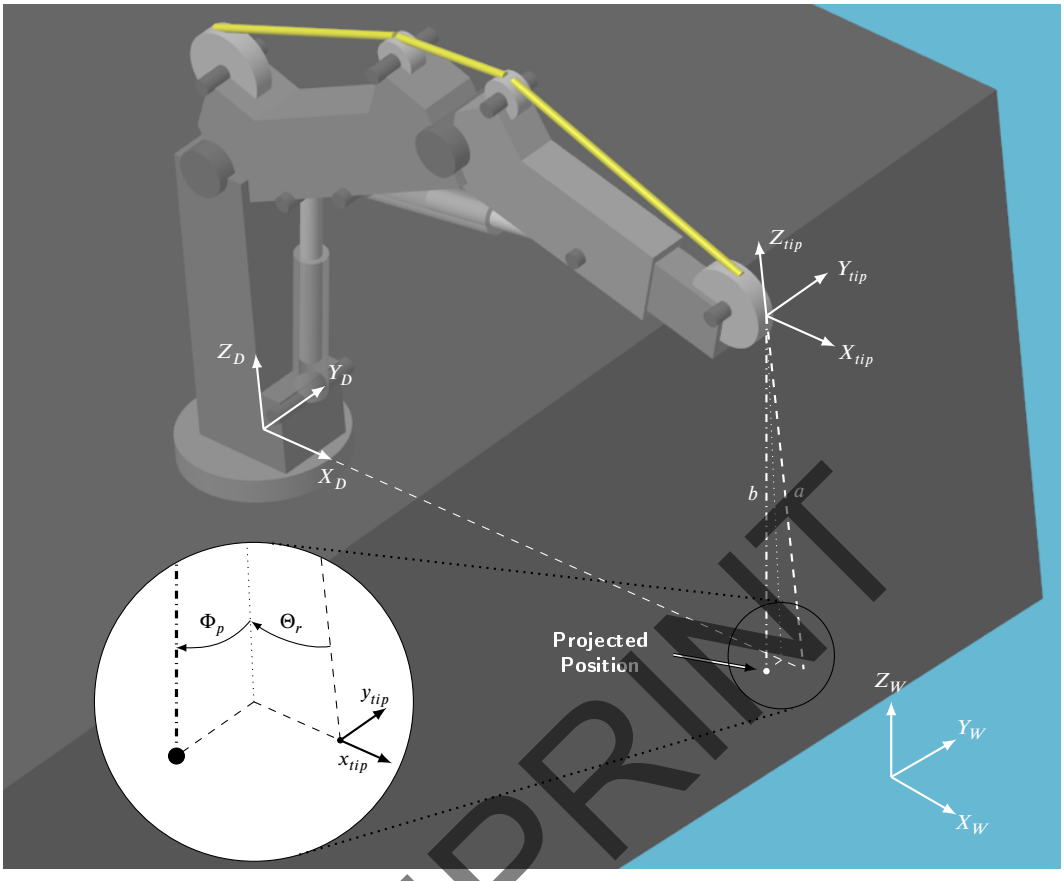

Figure 7: The projected position of the payload in the XY_D plane, required for the calculation of z_{WF}, where XYZ_D is the deck coordinate frame, XYZ_{tip} is the tip coordinate frame, and XYZ_W is the world coordinate frame. For clarity, note that line a is colinear with Z_{tip}, while line b is colinear with Z_W.

displacement of x_{WF}, y_{WF} and z_{WF} from their initial values $x_{WF,lock}$, $y_{WF,lock}$ and $z_{WF,lock}$. In addition, to prevent sudden jumps in the payload position, a strength factor S_{WF} is used, scaling from zero to one during a specified time interval. In this study, the time interval is set to five seconds. Therefore, when world-frame compensation is activated, S_{WF} is set to zero and new values for $x_{WF,lock}$, $y_{WF,lock}$ and $z_{WF,lock}$ are captured. The world-frame strength is then increased to one over a five second time interval. To return to deck-frame compensation, the value of S_{WF} is lowered from one to zero over another five-second interval.

In manual control, activating or de-activating world-frame compensation is controlled by a simple button press by the operator. For automated control, a threshold can be used to trigger activation of world-frame compensation; in this work, $z_d + z_{i,payload} < z_{thresh}$ was used as the threshold function, where $z_{i,payload}$ is the initial z position of the payload in the deck coordinate frame and z_{thresh} is the threshold height above the ship deck.

4. Simulation Case Studies

To emulate real-time deployment, the anti-sway system was programmed in LabVIEW and deployed to a National Instrument myRIO, operating at a frequency of 100 Hz. To simulate the dynamics of the crane and ship, the MATLAB extension Simscape Multibody was used, which communicated with LabVIEW via a UDP connection. To simplify testing, kinematic control was used for the actuators, emulating a well-tuned hydraulic control system with counterbalance valves. The ship motion used in all of the simulations was generated with ShipMo3D, a validated software package [13, 14]. Sea state 6 was used in the simulation, where Table 1 provides the root-mean-squared parameters. The sea way was modelled with regular waves of the Bretschneider spectrum, with a significant wave height of of 5 metres and a period of 12.4 seconds. The ship used was the generic frigate, with a length of 120 m, and

Table 1
Ship Motion Parameters

	Surge (m)	Sway (m)	Heave (m)	Roll (°)	Pitch (°)	Yaw (°)
RMS	0.701	0.197	0.908	1.360	1.600	0.244

sailed at a speed of 6.000 kt with a heading of 15.0° into the sea. The frequency of the ship's roll, pitch and yaw motion was 0.093 Hz.

In Section 4.1, the system will be tasked with tracking a pre-defined, automated trajectory to demonstrate the performance of the anti-sway system under repeatable conditions. Operator-in-the-loop tests and a thorough human factors study has been left for future work; however, to facilitate such testing, the system has been designed for real-time operator input. In Section 4.2, the system will track the same trajectory in the presence of wind disturbances, as well as with two different payload masses; the utility of the self-tuning system in counteracting the wind disturbances and variable payload masses will be investigated. Finally, in Section 4.3 the effect of the double pendulum on system performance will be investigated. Video animations of several tests are provided in the supplementary files.

4.1. Automated Trajectory

In the first case study, the system is tasked with tracking a pre-defined, time-varying trajectory for the payload:

$$\dot{x}_d = \begin{cases} 0.1 \text{ m/s} & 5 \text{ s} < t < 25 \text{ s} \\ -0.1 \text{ m/s} & 90 \text{ s} < t < 100 \text{ s or } 110 \text{ s} < t < 120 \text{ s} \\ 0 & \text{otherwise} \end{cases} \tag{33}$$

$$\dot{y}_d = \begin{cases} 0.1 \text{ m/s} & 5 \text{ s} < t < 25 \text{ s} \\ -0.1 \text{ m/s} & 70 \text{ s} < t < 100 \text{ s or } 110 \text{ s} < t < 120 \text{ s} \\ 0 & \text{otherwise} \end{cases} \tag{34}$$

$$\dot{z}_d = \begin{cases} 0.1 \text{ m/s} & 5 \text{ s} < t < 15 \text{ s or } 100 \text{ s} < t < 120 \text{ s} \\ -0.2 \text{ m/s} & 40 \text{ s} < t < 60 \text{ s} \\ 0 & \text{otherwise} \end{cases} \tag{35}$$

Figure 8 shows the resulting payload position after integrating the pre-defined payload trajectory, relative to the payload's initial position. Figure 8 also shows five screenshots of the system during operation. The initial crane states are $\theta_0 = 0$ rad, $d_1 = 1.25$ m, $d_2 = 0.5$ m, $d_3 = 0$ m and $l_8 = 1.5$ m, which results in an initial payload z coordinate $z_{i,payload} = 1.159$ m. Therefore, since z_d starts at zero and using $z_{thresh} = -1$ m, or one metre below the ship deck, the system will start in deck-frame compensation mode, as $z_d + z_{i,payload} >= z_{thresh}$. Following the given trajectory, the system will switch to world-frame compensation at $t = 55.9$ s into the simulation, reaching full world-frame compensation five seconds after at $t = 60.9$ s. The system will then switch back to deck-frame compensation at $t = 108.5$ s.

The mass of the payload was 1770 kg, approximately the mass of a small Zodiac-style watercraft [30], and the remaining crane parameters are provided in Appendix A. The self-tuning gains chosen for the simulation were tuned heuristically to minimize payload tracking root-mean-square error (RMSE), and set to $\varrho_x = \varrho_y = 0.0001$ and $\Gamma_x = \Gamma_y = 0.001$. The remaining constants were set to $k_1 = 4$, $k_2 = 50$, $\epsilon_1 = \epsilon_2 = 0.1$, $\epsilon_3 = 0.001$.

Figure 9 shows the x, y and z position of the payload as a function of time in the deck coordinate frame, relative to the initial payload position, while Figure 10 shows the x, y and z position of the payload, in the same simulation, but in the world coordinate frame. The darker-grey sections of the figures indicate the transition periods between deck and world-frame compensation, while the lighter-grey sections indicate that the opposite compensation system is active. Each "section" of Figures 9 and 10 are given a unique designation; sections a, b and c correspond to the payload position measured in the deck-frame (Figure 9), where in sections a and c deck-frame compensation is active, while in section b world-frame compensation is active. Likewise sections d, e and f correspond to the payload position measured in

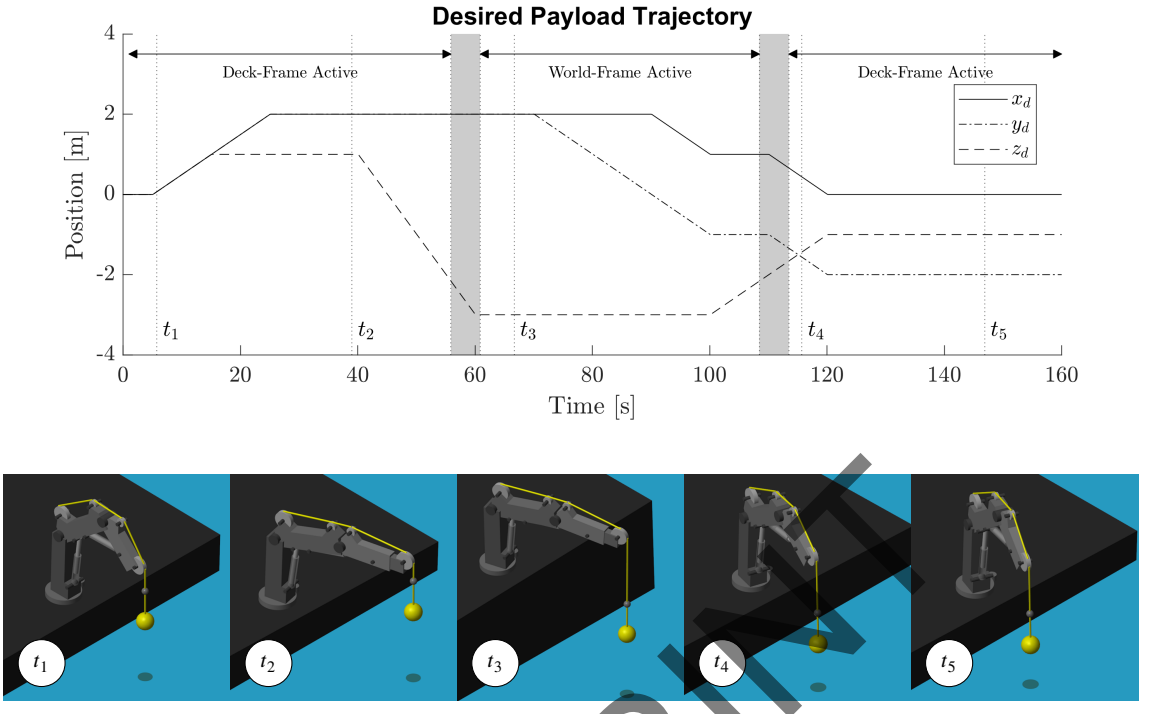

Figure 8: The desired payload trajectory (upper), and screenshots of the simulation during the test (lower).

Table 2
The root-mean-square-errors (RMSE) for the automated trajectory trial. The percent improvements for sections *a* and *c* are relative to section *b*, while the percent improvement for section *e* is relative to the average of sections *d* and *f*.

Compensation Mode	Section	RMSE (m) x	y	z	Average	Percent Improvement (%)
Deck	*a*	0.0136	0.0305	0.0053	0.0164	98.73[1]
	b	0.3691	1.2370	2.2850	1.2970	—
	c	0.0152	0.0331	0.0037	0.0173	98.66[1]
World	*d*	0.3357	1.1281	2.2772	1.2470	—
	e	0.0869	0.1377	0.0510	0.0919	92.70[2]
	f	0.3557	1.1802	2.2716	1.2692	—

[1] Percent improvement of the average RMSE of sections *a* or *c* relative to the average RMSE of section *b*.
[2] Percent improvement of the average RMSE of section *e* relative to the combined average RMSE of sections *d* and *f*.

the world-frame (Figure 10), where again in sections *d* and *f* deck-frame compensation is active, while in section *e* world-frame compensation is active.

It is expected that in sections *b*, *d* and *f* the system will show reduced performance, as in these sections the system will be using the opposing compensation mode. In practice, an operator could manually switch modes depending on the requirements of the marine crane operation to ensure the correct compensation mode is active. Likewise, the automatic switching system is designed to switch to world-frame compensation as the payload is off-boarded and lowered to ocean surface, and switch back to deck-frame compensation as the payload is hoisted aboard the ship.

Figure 11 shows the error between the desired and actual trajectories in both the deck and world coordinate frames, and Table 2 shows the average root-mean-square-errors (RMSEs) during the simulation in each of the six sections. The average RMSEs were calculated by averaging the RMSE of the *x*, *y* and *z* trajectories calculated across the entire time-span of the corresponding section; the transition zones were not included in any of the average RMSEs.

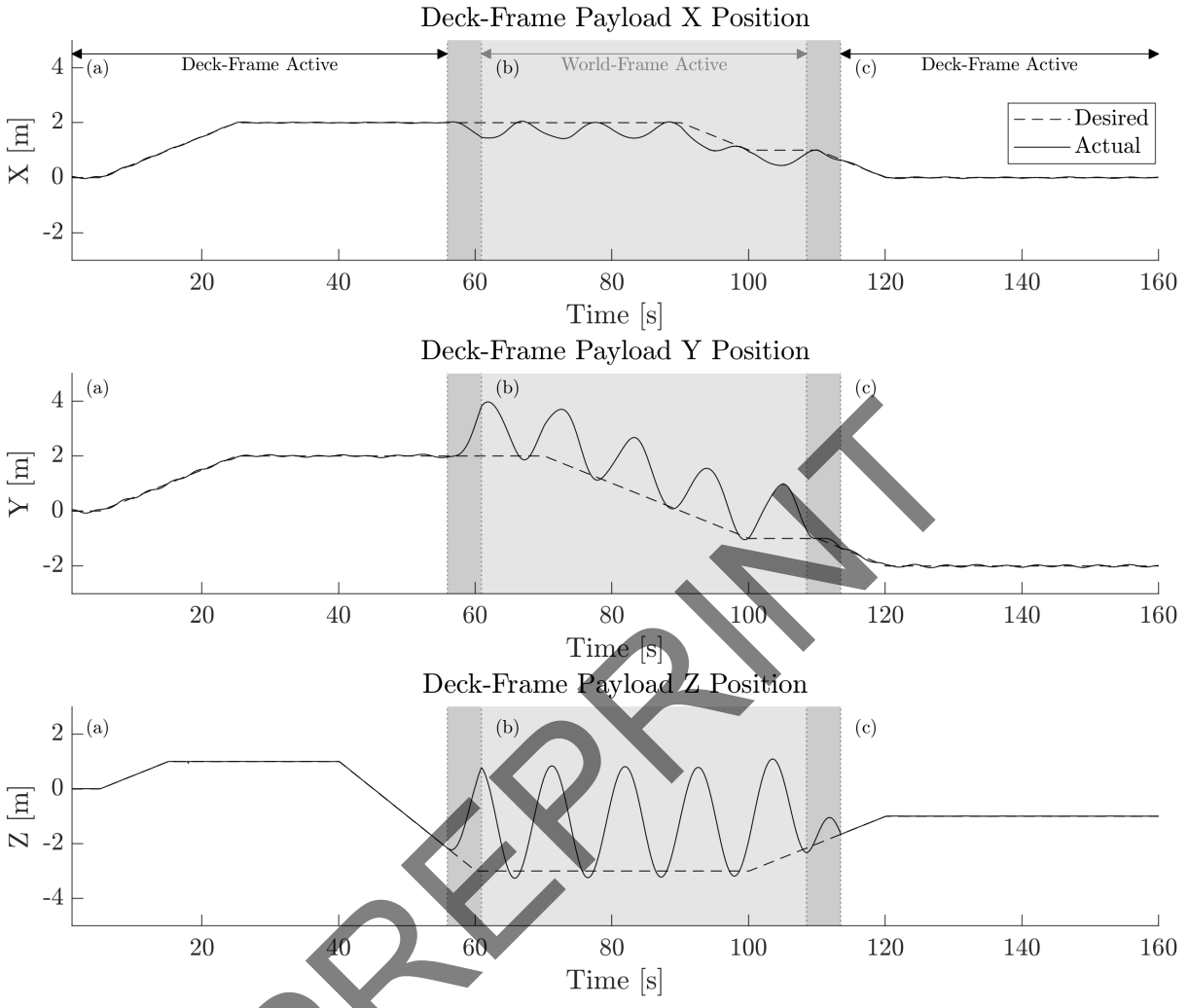

Figure 9: The position of the payload in the deck coordinate frame during the automated simulation, relative to the payload's initial position. The darker-grey sections indicate the transition periods between deck and world-frame compensation, while the lighter-grey sections indicate that the opposing compensation system is active.

Figure 11 and Table 2 show that the system tracking performance is significantly improved when the corresponding compensation mode is active. Activating deck-frame compensation shows a 98.73% and 98.66% reduction in deck-frame error in sections *a* and *c* compared to section *b*, where world-frame compensation is active. Activating world-frame compensation shows a 92.70% reduction in world-frame error in section *e* compared to sections *d* and *f*, where deck-frame compensation is active. The results show that activating the corresponding compensation mode significantly reduces undesired payload motion relative to the ocean surface (world-frame compensation) or the ship deck (deck-frame compensation), depending on the operator's preference.

While the world-frame compensation system has a larger average RMSE of 0.0919 m (while active) compared to the deck-frame compensation RMSEs of 0.0164 m and 0.0173 m (while active), all average RMSEs are significantly reduced when the corresponding compensation mode is activated. The larger average RMSE of the world-frame while active compared to the deck-frame could be attributed to the increased motion of the crane; when deck-frame compensation was active, the average speed of the five crane actuators was 0.0254 m/s, while when ocean-frame

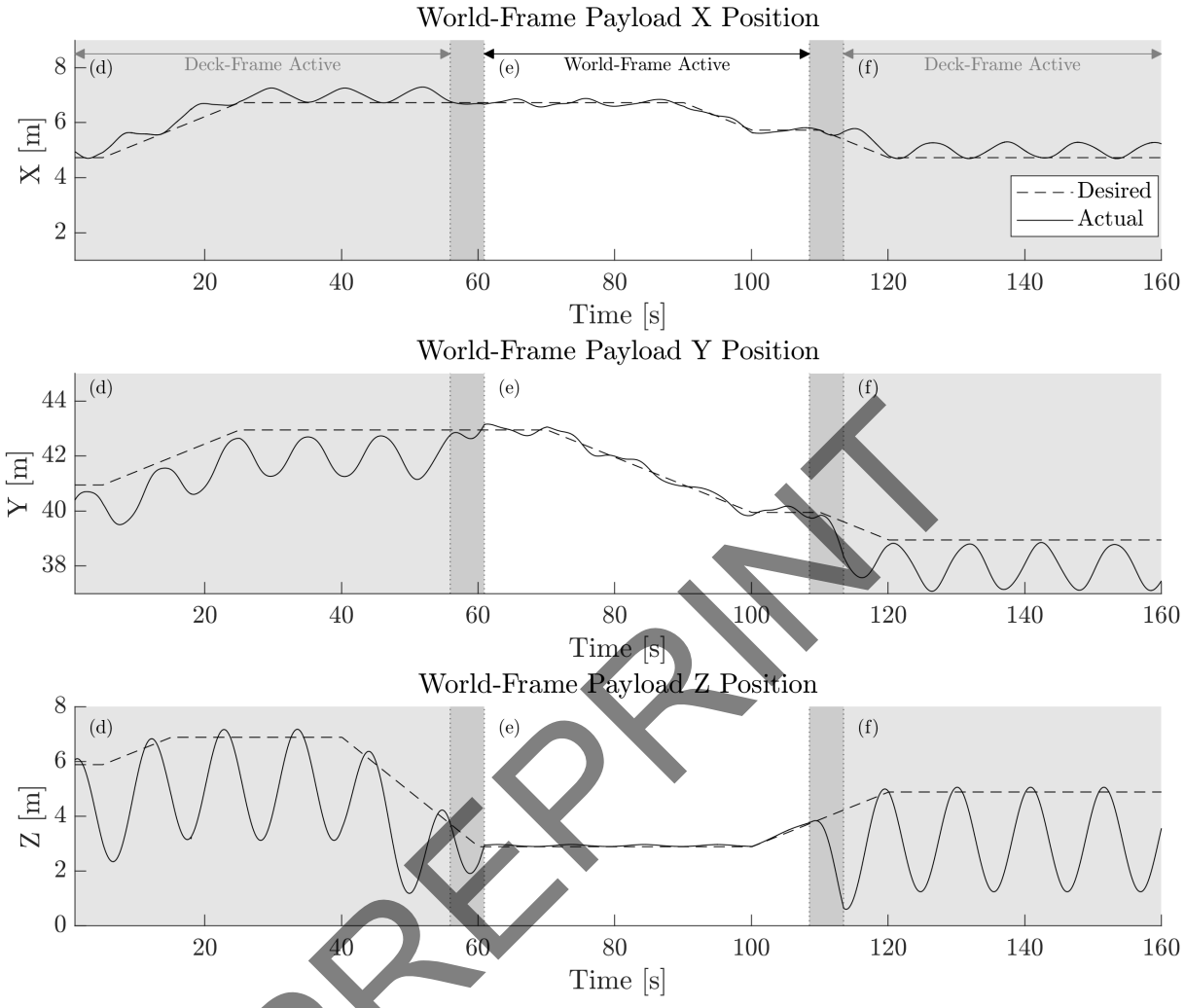

Figure 10: The position of the payload in the world coordinate frame during the automated simulation, relative to the ship's IMU. The darker-grey sections indicate the transition periods between deck and world-frame compensation, while the lighter-grey sections indicate that the opposing compensation system is active.

compensation was active, the average speed of the five actuators was over five times more at 0.1365 m/s in order to counteract the ship's motion. The significantly increased motion of the crane and crane tip resulted in additional kinetic energy transfer to the payload, which explains the slightly reduced performance in world-frame compensation compared to deck-frame compensation.

The above study is disturbance free; thus, one needs to consider the effect of wind in the high fidelity simulations.

4.2. Wind Disturbances

The wind disturbances were modelled using the Dryden wind model [12], using a nominal relative wind speed of 18 m/s. The Dryden model provided a wind speed vector $\mathbf{v}_{wind}$ acting on the payload, where using the ship's heading of 15°, resulted in RMS wind speeds of 3.926 m/s in the world x direction, 14.58 m/s in the world y direction, and

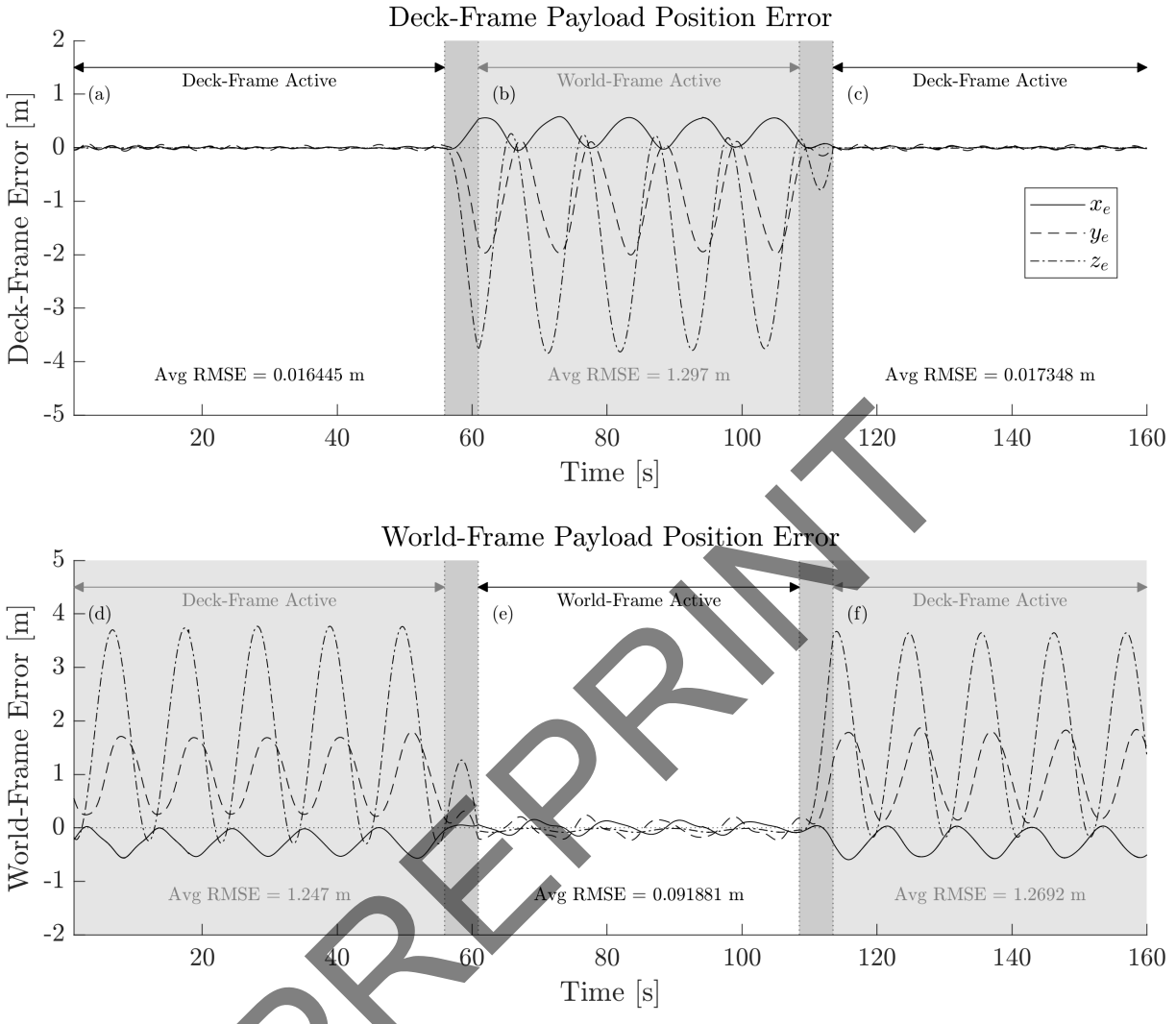

Figure 11: The error between the desired and actual payload position in the deck coordinate frame (upper) and world coordinate frame (lower) during the automated simulation. The darker-grey sections indicate the transition periods between deck and world-frame compensation, while the lighter-grey sections indicate that the opposing compensation system is active.

0.393 m/s in the world z direction. The force vector $\mathbf{F}_{dist}$ applied on the payload was then calculated using

$$\mathbf{F}_{dist} = PA = \frac{A\rho(\mathbf{v}_{wind})^2}{2} \tag{36}$$

where P is the wind pressure, A is the projected surface area of the payload, in this work assumed for simplicity to be a circle of radius 0.75 m, and $\rho = 1.225$ kg/m^3 the density of air at sea level [2]. The resulting RMS disturbance forces were 17.41 N, 233.7 N and 0.3096 N in the world x, y and z directions.

To test the disturbance rejection performance of the system, simulations were run both with and without wind disturbances, along with two different types of payloads: the "heavy" 1770 kg payload, as was used in Section 4.1, as well as a "light" 450 kg payload, intended to represent a large buoy. Both payloads were considered to have the same

Table 3
The average payload root-mean-square-errors (RMSE) across the x, y and z axes for the wind disturbance trials. The percent improvements are all relative to the "control" case, with a negative value indicating the payload tracking error was poorer than the control case. The heavy payload has a mass of 1770 kg, while the light payload has a mass of 450 kg.

Self-Tuning?	Wind?	Payload Type	RMSE (m)	Percent Improvement (%)
Yes	No	**Heavy**[1]	**0.0546**	—
		Light	0.0503	7.85
	Yes	Heavy	0.0545	0.04
		Light[2]	0.0550	-0.73
No	No	Heavy	0.0567	-3.90
		Light	0.0542	0.71
	Yes	Heavy	0.0638	-16.84
		Light[3]	0.1098	-101.17

[1] Control case, same as used in Section 4.1.
[2] Case 2 shown on Figure 12.
[3] Case 3 shown on Figure 12.

surface area. Each case was also tested both with and without self-tuning for the trajectory modifier gains ξ_x, ξ_y, Υ_x and Υ_y.

Table 3 shows the average RMSE of the eight simulations, taken across sections *a*, *e*, and *c*, which had the correct compensation mode active. Figure 12 shows the root-square-error (RSE) of the control case, which had no wind, self-tuning and the heavy payload (identical to the simulation in Section 4.1), as well as the cases with the light payload and wind, both with and without self-tuning. The cases shown in Figure 12 are identified on Table 3 by superscripts.

With self-tuning active, there was very little relative change in performance, regardless of whether wind disturbances were present or which payload was in use; with wind included, the largest decrease in performance was only 0.73%. However, if self-tuning was disabled, a much larger decrease in performance was observed, with a maximum of 101.17% when the light payload was used in the presence of wind disturbances. The results therefore show that self-tuning is highly effective at minimizing the effect of both wind disturbances and a variable payload mass.

To help address the noted deficinecy of the double pendulum models in marine crane anti-sway [1], the high-fidelity simulator was used to analyze any effects to the anti-sway system caused by the double pendulum.

4.3. Double Pendulum Effects

In all the previous trials, the knuckle boom crane featured the double pendulum and 9 degrees of freedom. To investigate if the double pendulum caused a significant impact on anti-sway performance, the knuckle boom crane was reduced to only 7 degrees of freedom by locking the universal joint at the hook, resulting in a single pendulum, as shown in Figure 13. No other alterations to the dynamic model or control system were made.

The same trials were run as in Section 4.2, with wind disturbances, for both the double and single pendulum case, with the payload RMSE results shown in Table 4. The maximum percent difference in tracking accuracy was only 1.12%, with a resulting difference on the order of millimetres. Therefore, the double pendulum did not appear to have a significant impact on anti-sway performance for our system within simulation; however, interested readers may wish to consult the work of Sun et al. [23], who developed a control system for a planar boom crane specifically to counteract double pendulum effects.

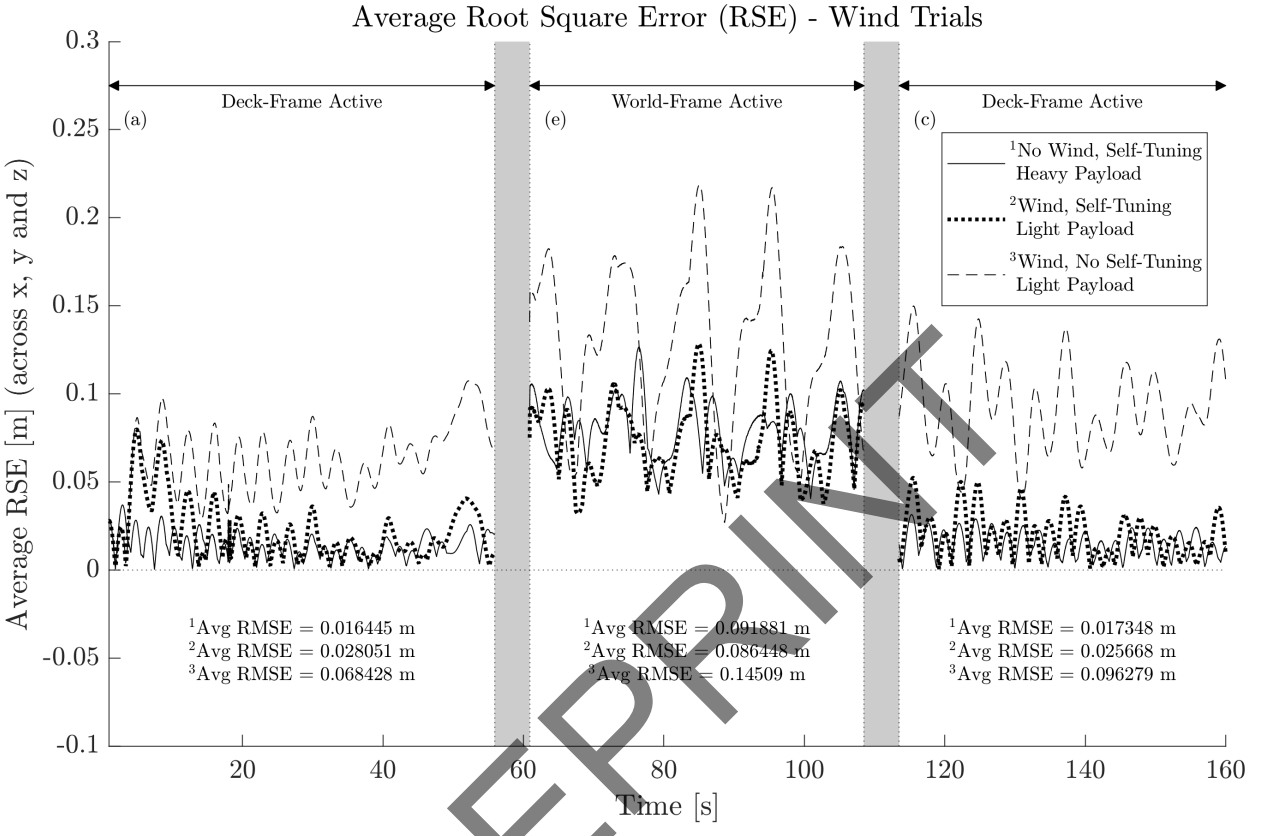

Figure 12: The root-square-error (RSE) of the payload during the wind trials. Note that only sections *a*, *c* and *e* are shown, as those sections correspond to when the correct compensation mode is active.

Table 4
The payload root-mean-square-errors (RMSE) across the x, y and z axes both with the double pendulum and the single pendulum. The heavy payload has a mass of 1770 kg, while the light payload has a mass of 450 kg.

Self-Tuning?	Payload Type	RMSE (m)		Percent Difference (%)
		Double Pendulum	Single Pendulum	
Yes	Heavy	0.0545	0.0543	0.38%
	Light	0.0550	0.0544	1.12%
No	Heavy	0.0638	0.0636	0.22%
	Light	0.1098	0.1089	0.80%

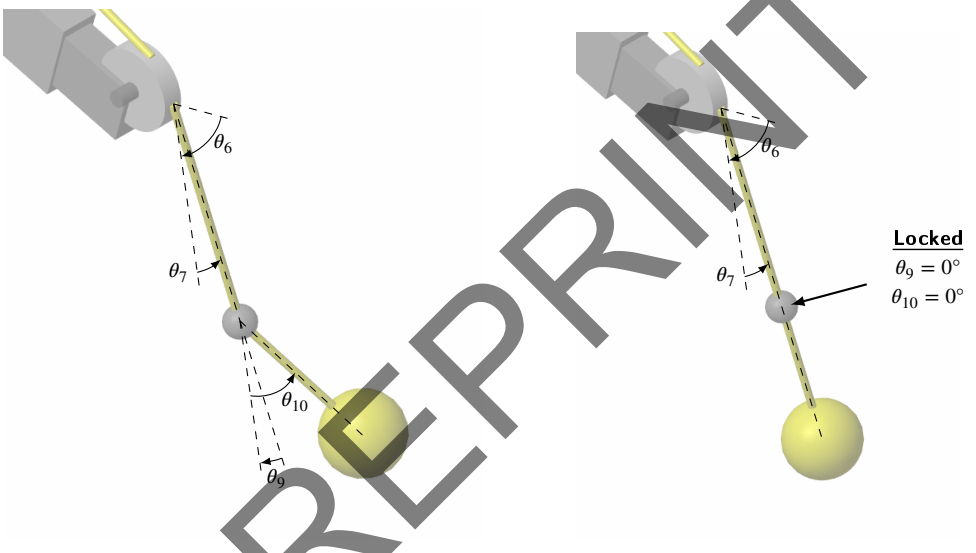

(a) The double pendulum has four sway angles θ_6, θ_7, θ_9 and θ_{10}.

(b) The single pendulum only has two sway angles, θ_6 and θ_7.

Figure 13: The double and single pendulum cables.

5. Conclusion

In this work, a self-tuning anti-sway system was developed that can provide full motion compensation for the payload in either the deck or world (ocean) coordinate frames. The system is capable of real-time operator input, where the operator can provide a payload trajectory via a three-axes Cartesean input, rather than independent joint control. The system was applied to a 9-DOF shipboard knuckle boom crane, which featured double pendulum dynamics between the hook and payload, and was tested with full 6-DOF ship motion at sea state 6.

In the deck frame, the self-tuning anti-sway system showed a minimum percent improvement in payload tracking RMSE of 98.66%, while in the world frame, the system showed a percent improvement of 92.70%, both significant reductions. Additionally, when tested in the presence of wind disturbances and with two different payload masses, the self-tuning system showed only a 0.73% maximum decrease in performance; in contrast, with self-tuning disabled, the system showed a 101.17% decrease in performance. Therefore, the self-tuning anti-sway control system developed in this work has been shown to be highly effective at reducing payload tracking error in both the deck and world coordinate frames, in the presence of wind disturbances and variable payload masses. Additionally, the effect of the double pendulum was investigated through a comparison with a single pendulum; it was found that there was only a maximum percent difference of 1.12%, indicating that the double pendulum did not have a significant impact on anti-sway performance for our system in simulation.

While it is assumed in this work that the Cartesian control system will be more intuitive for the operator than individual joint control, future work will involve real-time operator-in-the-loop testing to further validate the system and investigate the human factors of anti-sway control.

Acknowledgment

The authors acknowledge the support of the Natural Sciences and Engineering Research Council of Canada (NSERC), [funding reference number RGPIN-2017-06967]. Cette recherche a été financée par le Conseil de recherches en sciences naturelles et en génie du Canada (CRSNG), [numéro de référence RGPIN-2017-06967]. Additionally, we would like to acknowledge Carleton University for their support. The authors would like to thank DSA LTD (Dynamic Systems Analysis Ltd) for the in-kind donation of ShipMo3D.

CRediT authorship contribution statement

Iain A. Martin: Methodology, Software, Investigation, Validation, Formal analysis, Writing - Original Draft, Visualization. **Rishad A. Irani:** Conceptualization, Resources, Investigation, Data Curation, Writing - Review & Editing, Supervision, Project Administration, Funding Acquisition.

References

[1] Cao, Y., Li, T., 2020. Review of antiswing control of shipboard cranes. IEEE/CAA Journal of Automatica Sinica 7(2), 346–354.
[2] Çengal, Y., Cimbala, J., 2016. Fluid Mechanics, Fundamentals and Applications. third ed., McGraw Hill Education.
[3] Galieriková, A., 2019. The human factor and maritime safety, in: 13th International Scientific Conference on Sustainable, Modern and Safe Transport (TRANSCOM 2019).
[4] Guo, B., Chen, Y., 2020. Fuzzy robust fault-tolerant control for offshore ship-mounted crane system. Information Sciences 256, 119–132.
[5] Ismail, R., That, N., Ha, Q., 2015. Modelling and robust trajectory following for offshore container crane systems. Automation in Construction 59, 179–187.
[6] Kim, D., Park, Y., 1999. Tracking control in x-y plane of an offshore container crane. Trans. of the Society of Instrument and Control Engineers 35(2), 253–261.
[7] Kim, G., Hong, K., 2019. Adaptive sliding mode control of an offshore container crane with unknown disturbances. IEEE/ASME Transactions on Mechatronics .
[8] Lu, B., Fang, Y., Sun, N., 2019. Nonlinear coordination control of offshore boom cranes with bounded control inputs. International Journal of Robust Nonlinear Control 29, 1165–1181.
[9] Lu, B., et al., 2018. Antiswing control of offshore boom cranes with ship roll disturbances. IEEE Transactions on Control Systems Technology 26(2), 740–747.
[10] Martin, I., Irani, R., 2020. Dynamic modeling and self-tuning anti-sway control of a seven degree of freedom shipboard knuckle boom crane. Mechanical Systems and Signal Processing 153, 107441.
[11] Martin, I., Irani, R., 2021. A generalized approach to anti-sway control for shipboard cranes. Mechanical Systems and Signal Processing 148, 107168.

[12] MathWorks, . Dryden wind turbulence model (continuous). https://www.mathworks.com/help/aeroblks/drydenwindturbulencemodelcontinuous.html. Accessed: 2020-05-19.
[13] McTaggart, K., 2011. ShipMo3D version 3.0 user manual for computing ship motions in the time and frequency domains. Defense Research and Development Canada - Atlantic (DRDC - Atlantic). Dartmouth, Nova Scotia. TM 2011-308.
[14] McTaggart, K., 2012. Validation of ShipMo3D version 3.0 user applications for simulation ship motions. Defense Research and Development Canada - Atlantic (DRDC - Atlantic). Dartmouth, Nova Scotia. TM 2011-306.
[15] Ngo, Q., et al., 2017. Fuzzy sliding mode control of an offshore container crane. Ocean Engineering 140, 125–134.
[16] Nguyen, N., Ngo, Q., Ha, Q., 2015. Active control of an offshore container crane. 2015 International Conference on Control, Automation and Systems (ICCAS) .
[17] Qian, Y., Fang, Y., Lu, B., 2015. A learning strategy based partial feedback linearization control method for an offshore boom crane, in: 2015 IEEE Annual Conference on Decision and Control (CDC).
[18] Qian, Y., Fang, Y., Lu, B., 2017. Adaptive repetitive learning control for an offshore boom crane. Automatica 82, 21–28.
[19] Qian, Y., Fang, Y., Lu, B., 2019. Adaptive robust tracking control for an offshore ship-mounted crane subject to unmatched sea wave disturbances. Mechanical Systems and Signal Processing 114, 556–570.
[20] Ramli, L., et al., 2017. Control strategies for crane systems: A comprehensive review. Mechanical Systems and Signal Processing 95, 1–23.
[21] Sun, N., et al., 2018. Nonlinear antiswing control of offshore cranes with unknown parameters and persistent ship-induced perturbations: Theoretical design and hardware experiments. IEEE Transactions on Industrial Electronics 65(3), 2629–2641.
[22] Sun, N., et al., 2019a. Dynamic feedback antiswing control of shipboard cranes without velocity measurement: Theory and hardware experiments. IEEE Transactions on Industrial Informatics 15(5), 2879–2891.
[23] Sun, N., et al., 2019b. Nonlinear stable transportation control for double-pendulum shipboard cranes with ship-motion-induced disturbances. IEEE Transactions on Industrial Electronics 66(12), 9467–9479.
[24] Tysse, G., Egeland, O., 2018. Dynamic interaction of a heavy crane and a ship in wave motion. Modeling, Identification and Control 39(2), 45–60.
[25] Tysse, G., Egeland, O., 2019. Crane load position control using lyapunov-based pendulum damping and nonlinear MPC position control, in: Proceedings of The 18th European Control Conference (ECC).
[26] Wang, J., et al., 2021. Dynamic modeling and analysis of the telescopic sleeve antiswing device for shipboard cranes. Mathematical Problems in Engineering , 6685816.
[27] Wang, S., et al., 2018. Dynamic modelling and analysis of 3-axis motion compensated offshore cranes. Ships and Offshore Structures 13(3), 265–272.
[28] Yang, T., et al., 2020. Neural network-based adaptive antiswing control of an underactuated ship-mounted crane with roll motions and input dead zones. IEEE Transactions on Neural Networks and Learning Systems 31(3), 901–914.
[29] Zanjani, M., Mobayen, S., 2021. Anti-sway control of offshore crane on surface vessel using global sliding mode control. International Journal of Control , 1906447.
[30] Zodiac-Nautic.com, . Open 6.5. [Online]. Available: https://www.zodiac-nautic.com/en/shop/produits/boats/open-en/open-6-5. [Accessed: 15-Mar-2019].

A. Knuckle Boom Crane and Simulation Properties

Figure 14 shows the main dimensions of the knuckle boom crane, and Table 5 provides the relevant crane properties used in this work.

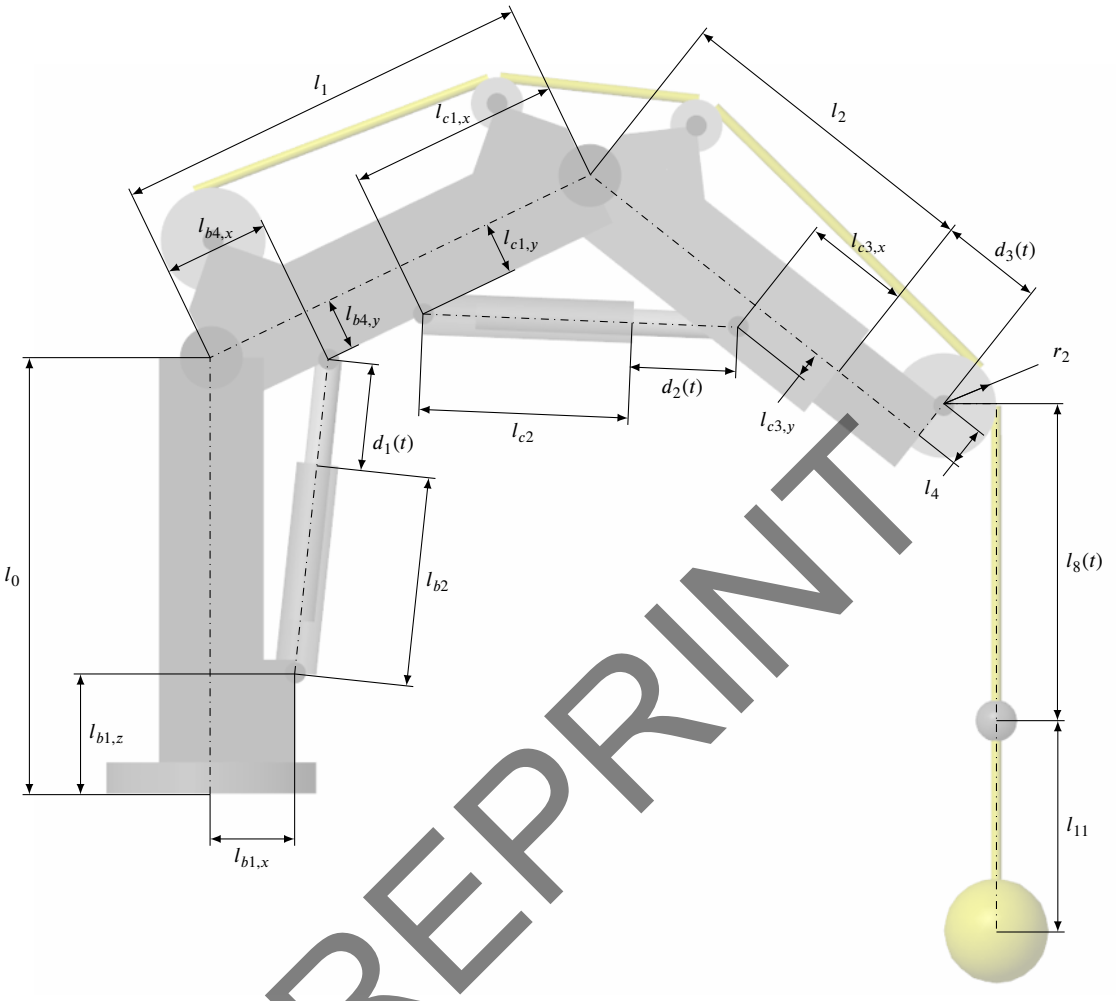

Figure 14: The main dimensions required in this work to parameterize the knuckle boom crane.

Table 5
Knuckle Boom Crane Model Parameters

Parameter	Value	Parameter	Value
l_0	4 m	$l_{c1,x}$	2 m
l_1	4 m	$l_{c1,y}$	0.5 m
l_2	3 m	$l_{c3,x}$	2 m
l_4	0.375 m	$l_{c3,y}$	0.5 m
l_{11}	2 m	l_{b2}	2 m
$l_{b1,x}$	0.8 m	l_{c2}	2 m
$l_{b1,z}$	1 m	r_2	0.5 m
$l_{b4,x}$	1 m	m_{hook}	100 kg
$l_{b4,y}$	0.5 m		

B. Crane Tip Forward Kinematics

Figure 15 shows the coordinate frames mapping from XYZ_D to the crane tip, which are the same as used in [10] and were assigned using the DH convention. The corresponding transformation matrices are

$$ {}^{D}T_1 = \begin{bmatrix} c(\theta_0) & 0 & -s(\theta_0) & 0 \\ s(\theta_0) & 0 & c(\theta_0) & 0 \\ 0 & -1 & 0 & l_0 \\ 0 & 0 & 0 & 1 \end{bmatrix}, \tag{37} $$

$$ {}^{1}T_2 = \begin{bmatrix} c(\theta_1(d_1)) & -s(\theta_1(d_1)) & 0 & l_1 c(\theta_1(d_1)) \\ s(\theta_1(d_1)) & c(\theta_1(d_1)) & 0 & l_1 s(\theta_1(d_1)) \\ 0 & 0 & 1 & 0 \\ 0 & 0 & 0 & 1 \end{bmatrix}, \tag{38} $$

$$ {}^{2}T_3 = \begin{bmatrix} c(\theta_2(d_2)) & -s(\theta_2(d_2)) & 0 & l_2 c(\theta_2(d_2)) \\ s(\theta_2(d_2)) & c(\theta_2(d_2)) & 0 & l_2 s(\theta_2(d_2)) \\ 0 & 0 & 1 & 0 \\ 0 & 0 & 0 & 1 \end{bmatrix}, \tag{39} $$

$$ {}^{3}T_4 = \begin{bmatrix} 1 & 0 & 0 & d_3 \\ 0 & 1 & 0 & 0 \\ 0 & 0 & 1 & 0 \\ 0 & 0 & 0 & 1 \end{bmatrix}, \tag{40} $$

$$ {}^{4}T_5 = \begin{bmatrix} c(-\pi/2) & -s(-\pi/2) & 0 & l_4 c(-\pi/2) \\ s(-\pi/2) & c(-\pi/2) & 0 & l_4 s(-\pi/2) \\ 0 & 0 & 1 & 0 \\ 0 & 0 & 0 & 1 \end{bmatrix}, \tag{41} $$

$$ {}^{5}T_6 = \begin{bmatrix} c(\theta_5) & -s(\theta_5) & 0 & r_2 c(\theta_5) \\ s(\theta_5) & c(\theta_5) & 0 & r_2 s(\theta_5) \\ 0 & 0 & 1 & 0 \\ 0 & 0 & 0 & 1 \end{bmatrix}. \tag{42} $$

Note that $\cos(\theta) = c(\theta)$ and $\sin(\theta) = s(\theta)$. Once concatenated, the components of the position vector of the crane tip $\mathbf{x}_{tip} = \begin{bmatrix} x_{tip} & y_{tip} & z_{tip} \end{bmatrix}^T$ in the deck coordinate frame are

$$ \begin{aligned} x_{tip} =& c(\theta_0)\Big[\Big[\big[r_2 s(\theta_5) + d_3 + l_2\big]c(\theta_2(d_2)) + \big[r_2 c(\theta_5) + l_4\big]s(\theta_2(d_2)) + l_1\Big]c(\theta_1(d_1)), \\ & - \Big[\big[-r_2 c(\theta_5) - l_4\big]c(\theta_2(d_2)) + \big[r_2 s(\theta_5) + d_3 + l_2\big]s(\theta_2(d_2))\Big]s(\theta_1(d_1))\Big] \end{aligned} \tag{43} $$

$$ \begin{aligned} y_{tip} =& s(\theta_0)\Big[\Big[\big[r_2 s(\theta_5) + d_3 + l_2\big]c(\theta_2(d_2)) + \big[r_2 c(\theta_5) + l_4\big]s(\theta_2(d_2)) + l_1\Big]c(\theta_1(d_1)), \\ & - \Big[\big[-r_2 c(\theta_5) - l_4\big]c(\theta_2(d_2)) + \big[r_2 s(\theta_5) + d_3 + l_2\big]s(\theta_2(d_2))\Big]s(\theta_1(d_1))\Big] \end{aligned} \tag{44} $$

$$ \begin{aligned} z_{tip} =& \Big[\big[-r_2 s(\theta_5) - d_3 - l_2\big]c(\theta_2(d_2)) + \big[-r_2 c(\theta_5) - l_4\big]s(\theta_2(d_2)) - l_1\Big]s(\theta_1(d_1)) \\ & + \Big[\big[r_2 c(\theta_5) + l_4\big]c(\theta_2(d_2)) - \big[r_2 s(\theta_5) + d_3 + l_2\big]s(\theta_2(d_2))\Big]c(\theta_1(d_1)) + l_0. \end{aligned} \tag{45} $$

In order to evaluate $\mathbf{x}_{tip}$ using the actuator extensions, expressions are needed for $\theta_1(d_1)$ and $\theta_2(d_2)$, as well as the cable fall angle θ_5. Figures 16a and 16b show the required geometry to calculate $\theta_1(d_1)$ and $\theta_2(d_2)$. The expressions

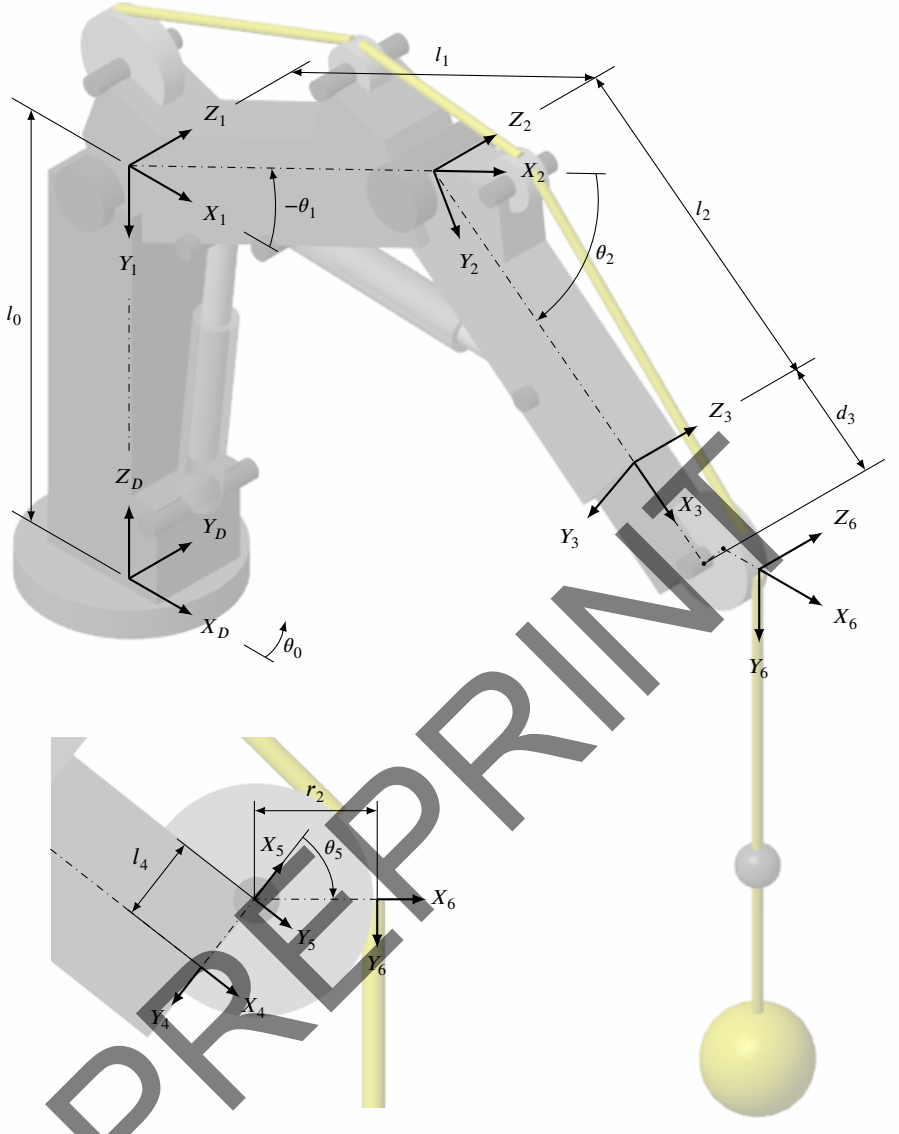

Figure 15: The coordinate frames for the forward kinematics of the crane tip.

for $\theta_1(d_1)$ and $\theta_2(d_2)$ are [10]

$$\theta_1(d_1) = \frac{\pi}{2} - \cos^{-1}\left(\frac{b_1^2 + b_4^2 - (d_1 + l_{b2})^2}{2b_1 b_4}\right) - \tan^{-1}\left(\frac{l_{b1,x}}{l_0 - l_{b1,z}}\right) - \tan^{-1}\left(\frac{l_{b4,y}}{l_{b4,x}}\right), \tag{46}$$

$$\theta_2(d_2) = \pi - \cos^{-1}\left(\frac{c_1^2 + c_3^2 - (d_2 + l_{c2})^2}{2c_1 c_2}\right) - \tan^{-1}\left(\frac{l_{c1,y}}{l_{c1,x}}\right) - \tan^{-1}\left(\frac{l_{c3,y}}{l_{c3,x}}\right), \tag{47}$$

where

$$b_1 = \sqrt{l_{b1,x}^2 + (l_0 - l_{b1,z})^2}, \tag{48}$$

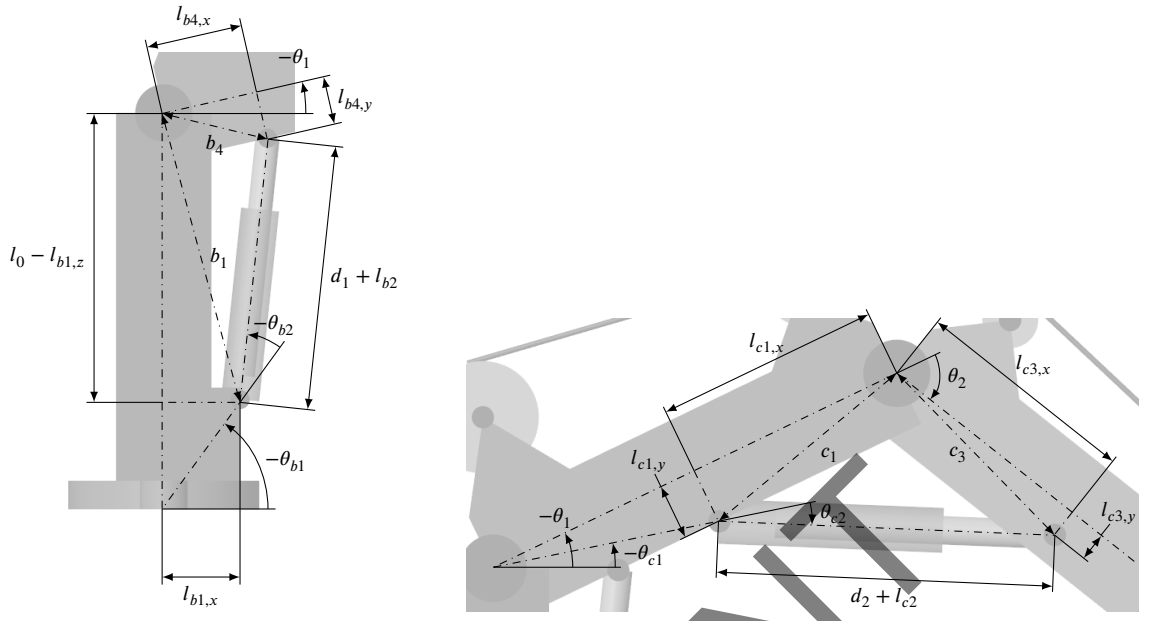

(a) The geometry required to determine θ_1 [10].

(b) The geometry required to determine θ_2 [10].

Figure 16: The geometry required for the intermediate angles.

$$b_4 = \sqrt{l_{b4,x}^2 + l_{b4,y}^2}, \tag{49}$$

$$c_1 = \sqrt{l_{c1,x}^2 + l_{c1,y}^2}, \tag{50}$$

$$c_2 = \sqrt{l_{c3,x}^2 + l_{c3,y}^2}. \tag{51}$$

The derivation of θ_5 is more involved, and the reader is referred to [10] for details. The final expression for θ_5 is [10]

$$\theta_5 = \theta_{5a} + \theta_{5b}, \tag{52}$$

where

$$\theta_{5a} = \frac{\pi}{2} - \theta_1(d_1) - \theta_2(d_2), \tag{53}$$

$$\theta_{5b} = \frac{\pi}{2} - \cos^{-1}\left[\sin(\Theta_r)\cos(\Phi_p)\cos(\theta_0) + \sin(\Phi_p)\sin(\theta_0)\right]. \tag{54}$$

C. Trajectory Integrator

The desired trajectory $\dot{\mathbf{x}}_d$ is integrated to produce the integrated desired trajectory $\mathbf{x}_d$ using

$$\mathbf{x}_d = \begin{cases} \frac{\dot{\mathbf{x}}_{d,i} + \mathbf{x}_{d,(i-1)}}{2}\Delta t & \text{if } ||x_e||_{i-1} < \epsilon_1 \\ \frac{\dot{\mathbf{x}}_{d,i} + \mathbf{x}_{d,(i-2)}}{2}\Delta t & \text{if } ||x_e||_{i-1} \geq \epsilon_1 \end{cases} \tag{55}$$

where i is the current timestep, $\Delta t = \frac{1}{f}$, where f is the sample rate, $||x_e||_{i-1}$ is the optimizer tracking error from the previous timestep and ϵ_1 is an error threshold. The purpose of the integrator is to limit the trajectory in the event the crane is driven beyond its range of motion; the actuator optimizer will attempt to find actuator extensions that can produce the desired trajectory, with the resulting optimized actuator setpoints producing an error $||x_e||$. If this error is

above an error threshold ϵ_1, the system interprets the desired trajectory as pushing the crane out of range. If this occurs, in the next timestep the system will integrate using the trajectory before being driven out of range, $\mathbf{x}_{d,(i-2)}$, rather than the trajectory from the previous timestep $\mathbf{x}_{d,(i-1)}$. In this way, the crane will continue to move if the operator alters their input to provide a trajectory that is within the range of motion of the crane.

D. Actuator Optimizer Equations

The inverse gradient for the *Jib* function is

$$\left[\nabla_{Jib}\right]^{-1} = \begin{bmatrix} G_{J11} & G_{J12} & G_{J13} \\ G_{J21} & G_{J22} & G_{J23} \\ G_{J31} & G_{J32} & G_{J33} \end{bmatrix} \tag{56}$$

where

$$\begin{aligned} G_{J11} =& -s(\theta_0)/\Big[\Big[\big[r_2 s(\theta_5)+d_3+l_2\big]c(\theta_2(d_2))+\big[r_2 c(\theta_5)+l_4\big]s(\theta_2)+l_1\Big]c(\theta_1(d_1)) \\ & -\Big[\big[-r_2 c(\theta_5)-l_4\big]c(\theta_2(d_2))+\big[r_2 s(\theta_5)+d_3+l_2\big]s(\theta_2(d_2))\Big]s(\theta_1(d_1))\Big] \end{aligned} \tag{57}$$

$$\begin{aligned} G_{J12} =& c(\theta_0)/\Big[\Big[\big[r_2 s(\theta_5)+d_3+l_2\big]c(\theta_2(d_2))+\big[r_2 c(\theta_5)+l_4\big]s(\theta_2)+l_1\Big]c(\theta_1(d_1)) \\ & -\Big[\big[-r_2 c(\theta_5)-l_4\big]c(\theta_2(d_2))+\big[r_2 s(\theta_5)+d_3+l_2\big]s(\theta_2(d_2))\Big]s(\theta_1(d_1))\Big] \end{aligned} \tag{58}$$

$$G_{J13} = 0 \tag{59}$$

$$\begin{aligned} G_{J21} =& c(\theta_0)\Big[\big[c(\theta_1(d_1))(r_2 c(\theta_5)+l_4)-(r_2 s(\theta_5)+d_3+l_2)s(\theta_1(d_1))\big]s(\theta_2(d_2)) \\ & +\big[(r_2 c(\theta_5)+l_4)s(\theta_1(d_1))+c(\theta_1(d_1))(r_2 s(\theta_5)+d_3+l_2)\big]c(\theta_2(d_2))\Big] \\ & /\left[\big[s(\theta_2(d_2))(r_2 s(\theta_5)+d_3+l_2)-(r_2 c(\theta_5)+l_4)c(\theta_2(d_2))\big]l_1\frac{\partial\theta_1}{\partial d_1}\right] \end{aligned} \tag{60}$$

$$\begin{aligned} G_{J22} =& s(\theta_0)\Big[\big[c(\theta_1(d_1))(r_2 c(\theta_5)+l_4)-(r_2 s(\theta_5)+d_3+l_2)s(\theta_1(d_1))\big]s(\theta_2(d_2)) \\ & +\big[(r_2 c(\theta_5)+l_4)s(\theta_1(d_1))+c(\theta_1(d_1))(r_2 s(\theta_5)+d_3+l_2)\big]c(\theta_2(d_2))\Big] \\ & /\left[\big[s(\theta_2(d_2))(r_2 s(\theta_5)+d_3+l_2)-(r_2 c(\theta_5)+l_4)c(\theta_2(d_2))\big]l_1\frac{\partial\theta_1}{\partial d_1}\right] \end{aligned} \tag{61}$$

$$\begin{aligned} G_{J23} =& \Big[\big[(-r_2 s(\theta_5)-d_3-l_2)c(\theta_1(d_1))-(r_2 c(\theta_5)+l_4)s(\theta_1(d_1))\big]s(\theta_2(d_2)) \\ & -\big[(-r_2 c(\theta_5)-l_4)c(\theta_1(d_1))+s(\theta_1(d_1))(r_2 s(\theta_5)+d_3+l_2)\big]c(\theta_2(d_2))\Big] \\ & /\left[\big[s(\theta_2(d_2))(r_2 s(\theta_5)+d_3+l_2)-(r_2 c(\theta_5)+l_4)c(\theta_2(d_2))\big]l_1\frac{\partial\theta_1}{\partial d_1}\right] \end{aligned} \tag{62}$$

$$\begin{aligned} G_{J31} =& -c(\theta_0)\Big[\big[c(\theta_1(d_1))(r_2 c(\theta_5)+l_4)-(r_2 s(\theta_5)+d_3+l_2)s(\theta_1(d_1))\big]s(\theta_2(d_2)) \\ & +\big[(r_2 c(\theta_5)+l_4)s(\theta_1(d_1))+c(\theta_1(d_1))(r_2 s(\theta_5)+d_3+l_2)\big]c(\theta_2(d_2))+c(\theta_1(d_1))l_1\Big] \\ & /\left[\big[s(\theta_2(d_2))(r_2 s(\theta_5)+d_3+l_2)-(r_2 c(\theta_5)+l_4)c(\theta_2(d_2))\big]l_1\frac{\partial\theta_2}{\partial d_2}\right] \end{aligned} \tag{63}$$

$$\begin{aligned} G_{J32} =& -s(\theta_0)\Big[\big[c(\theta_1(d_1))(r_2 c(\theta_5)+l_4)-(r_2 s(\theta_5)+d_3+l_2)s(\theta_1(d_1))\big]s(\theta_2(d_2)) \\ & +\big[(r_2 c(\theta_5)+l_4)s(\theta_1(d_1))+c(\theta_1(d_1))(r_2 s(\theta_5)+d_3+l_2)\big]c(\theta_2(d_2))+c(\theta_1(d_1))l_1\Big] \end{aligned}$$

$$/\left[\left[s(\theta_2(d_2))(r_2 s(\theta_5)+d_3+l_2)-(r_2 c(\theta_5)+l_4)c(\theta_2(d_2))\right]l_1\frac{\partial\theta_2}{\partial d_2}\right] \tag{64}$$

$$\begin{aligned} G_{J33} =&\Big[\left[(r_2 s(\theta_5)+d_3+l_2)c(\theta_1(d_1))+(r_2 c(\theta_5)+l_4)s(\theta_1(d_1))\right]s(\theta_2(d_2)) \\ &+\left[(-r_2 c(\theta_5)-l_4)c(\theta_1(d_1))+s(\theta_1(d_1))(r_2 s(\theta_5)+d_3+l_2)\right]c(\theta_2(d_2))+s(\theta_1(d_1))l_1\Big] \\ &/\left[\left[s(\theta_2(d_2))(r_2 s(\theta_5)+d_3+l_2)-(r_2 c(\theta_5)+l_4)c(\theta_2(d_2))\right]l_1\frac{\partial\theta_2}{\partial d_2}\right] \end{aligned} \tag{65}$$

The inverse gradient for the *Extension* function is

$$\left[\nabla_{Extension}\right]^{-1}=\begin{bmatrix} G_{E11} & G_{E12} & G_{E13} \\ G_{E21} & G_{E22} & G_{E23} \\ G_{E31} & G_{E32} & G_{E33} \end{bmatrix} \tag{66}$$

where

$$G_{E11} = G_{J11} \tag{67}$$

$$G_{E12} = G_{J12} \tag{68}$$

$$G_{E13} = G_{J13} \tag{69}$$

$$G_{E21} = -\frac{\left[c(\theta_2(d_2))s(\theta_1(d_1))+s(\theta_2(d_2))c(\theta_1(d_1))\right]c(\theta_0)}{\left[r_2 s(\theta_5)+l_1 c(\theta_2(d_2))+d_3+l_2\right]\frac{\partial\theta_1}{\partial d_1}} \tag{70}$$

$$G_{E22} = -\frac{\left[c(\theta_2(d_2))s(\theta_1(d_1))+s(\theta_2(d_2))c(\theta_1(d_1))\right]s(\theta_0)}{\left[r_2 s(\theta_5)+l_1 c(\theta_2(d_2))+d_3+l_2\right]\frac{\partial\theta_1}{\partial d_1}} \tag{71}$$

$$G_{E23} = \frac{-c(\theta_2(d_2))c(\theta_1(d_1))+s(\theta_2(d_2))s(\theta_1(d_1))}{\left[r_2 s(\theta_5)+l_1 c(\theta_2(d_2))+d_3+l_2\right]\frac{\partial\theta_1}{\partial d_1}} \tag{72}$$

$$\begin{aligned} G_{E31} =&c(\theta_0)\Big[\left[(r_2 s(\theta_5)+d_3+l_2)c(\theta_2(d_2))+(r_2 c(\theta_5)+l_4)s(\theta_2(d_2))+l_1\right]c(\theta_1(d_1)) \\ &-\left[(-r_2 c(\theta_5)-l_4)c(\theta_2(d_2))+s(\theta_2(d_2))(r_2 s(\theta_5)+d_3+l_2)\right]s(\theta_1(d_1))\Big] \\ &/\left[r_2 s(\theta_5)+l_1 c(\theta_2)+d_3+l_2\right] \end{aligned} \tag{73}$$

$$\begin{aligned} G_{E32} =&s(\theta_0)\Big[\left[(r_2 s(\theta_5)+d_3+l_2)c(\theta_2(d_2))+(r_2 c(\theta_5)+l_4)s(\theta_2(d_2))+l_1\right]c(\theta_1(d_1)) \\ &-\left[(-r_2 c(\theta_5)-l_4)c(\theta_2(d_2))+s(\theta_2(d_2))(r_2 s(\theta_5)+d_3+l_2)\right]s(\theta_1(d_1))\Big] \\ &/\left[r_2 s(\theta_5)+l_1 c(\theta_2)+d_3+l_2\right] \end{aligned} \tag{74}$$

$$\begin{aligned} G_{E33} =&\Big[\left[(-r_2 s(\theta_5)-d_3-l_2)s(\theta_1(d_1))+c(\theta_1(d_1))(r_2 c(\theta_5)+l_4)\right]c(\theta_2(d_2)) \\ &+\left[(-r_2 c(\theta_5)-l_4)s(\theta_2(d_2))-l_1\right]s(\theta_1(d_1))-s(\theta_2(d_2))c(\theta_1(d_1))(r_2 s(\theta_5)+d_3+l_2)\Big] \\ &/\left[r_2 s(\theta_5)+l_1 c(\theta_2)+d_3+l_2\right] \end{aligned} \tag{75}$$